applied sciences

MDPI

Article

Research on Double-Arc Cutting Tool Design and Cutting Performance

Mengchao Fan [1], Chunxu Bi [1], Caixu Yue [1], Xianli Liu [1,*] and Yingnan Zhu [2]

[1] Key Laboratory of Advanced Manufacturing and Intelligent Technology, Ministry of Education, Harbin University of Science and Technology, Harbin 150080, China
[2] Harbin Dongan Industrial Development Co., Ltd., Harbin 150066, China
* Correspondence: xianli.liu@hrbust.edu.cn; Tel.: +86-139-4511-1601

Featured Application: This research is beneficial to manufacturing applications.

Abstract: With the increasing complexity of the workpiece surfaces in aerospace and automotive molding and other areas, an increasing number of cutting tools with different shapes and performance have become necessary. A new kind of cutting tool is developed with a double-arc revolving surface at the tool's end to improve the processing quality in numerical control milling, referred to as a double-arc cutting tool (DACT) in this paper. The parametric geometric model of the DACT is established. Three types of cutting-edge curves are proposed (a cutting edge with a constant helix angle, a cutting edge with a constant pitch, and an orthogonal spiral cutting edge). Corresponding numerical simulation results are also provided as graphical representations. A DACT is manufactured and tested to verify its feasibility. Finally, two contrast experiments are conducted to prove that DACT has a higher processing quality than a ball-end mill (BEM). The advantage of the DACT is verified, which provides a theoretical basis for higher quality machining. The parametric design and application research provides a new method and theoretical basis for other new types of cutting tools.

Keywords: cutting tool design; tool manufacturing; double-arc cutting tool; cutting performance

check for updates

Citation: Fan, M.; Bi, C.; Yue, C.; Liu, X.; Zhu, Y. Research on Double-Arc Cutting Tool Design and Cutting Performance. *Appl. Sci.* **2023**, *13*, 3689. https://doi.org/10.3390/app13063689

Academic Editor: Jianlei Cui

Received: 17 February 2023
Revised: 3 March 2023
Accepted: 10 March 2023
Published: 14 March 2023

Copyright: © 2023 by the authors. Licensee MDPI, Basel, Switzerland. This article is an open access article distributed under the terms and conditions of the Creative Commons Attribution (CC BY) license (https://creativecommons.org/licenses/by/4.0/).

1. Introduction

With the rapid development of science and technology in the industrial manufacturing domain, people put forward higher and higher requirements for the quality of mechanical products. Therefore, cutting tools have received an increasing amount of attention, and solving the existing problems of cutting tools and making their design more innovative have become an important area of research [1]. BEM and ring mill cutters are widely used in the milling process and receive much attention [2]. At present, the main problems associated with the BEM are its low processing quality after machining, which not only leads to economic losses, but also affects the realization of the expected function [3]. Due to the limitations of geometry and structure, it is also difficult to solve the over-cutting and under-cutting problems of the ring mill cutter. Consequently, it is important to design and manufacture a new type of cutting tool that can address these issues.

In order to solve the existing problems associated with cutting tools, many scholars have improved and innovated cutting tools in various ways. Kandapr et al. [4] analyzed the optimal tool shape selection for the mass production of custom signs, and finally concluded that the shape of the surface geometry has a significant impact on the shape of the cutting tool required to machine a surface in order to ensure the processing quality. In order to solve the problem of low cutting efficiency, Otkur et al. [5] improved the milling path of cutting tools, proposing a double-cycloidal milling strategy that was tested in a three-axis vertical machining center. The experiments proved that this strategy can reduce the processing costs. Yang et al. [6] developed a damping tool by setting a single degree of freedom passive

damper inside the cutter bar. Finally, through experiments, it was proven that the damping tool could reduce the vibration generated by the tool during machining by avoiding the imbalance of the tool during high-speed rotation, so as to improve the surface quality of the workpiece after machining. Basso et al. [7] analyzed the influence of workpiece material and tool-face contact on the finishing of the BEM, and finally concluded that the finishing efficiency can be improved when the machining method used is reverse milling or the cutting mechanism is Tip-Out. Through experiments, Yang et al. [8] found that milling titanium alloy with a micro-texture cutter at an oblique angle could significantly affect the surface quality of the workpiece as well as the primary and secondary relationship between the micro-structure parameters of the cutter, the workpiece angle, and surface roughness. Cheng et al. [9] proposed a new mathematical model for an S-shaped cutting edge of the BEM considering the tooth offset center, which overcame the disadvantages of complex calculation and the poor adaptability of traditional modeling methods to facilitate the design of the BEM with better stability.

Masa et al. [10] successfully developed two types of BEM with a unique cutting edge, and verified that high finishing accuracy can be obtained by using the above-mentioned cutting tools. Li et al. [11] proposed a barrel ball-end mill (BBM) for blisk machining, and the result showed that the cutting efficiency of BBM increased more than three-fold compared to the BEM. Wang et al. [12] proposed a rotary cycloidal milling cutter with larger effective cutting helical angle and front angle than the BEM. When titanium alloys were used as the workpiece material, better machining efficiency was obtained using the rotary cycloidal milling cutter. Liu et al. [13] applied a micro-texture to the BEM for milling, provided a theoretical reference for determining the position of the micro-texture on the BEM, selected reasonable texture parameters, and provided a theoretical basis for improving the machining efficiency. Zhang et al. [14] proposed a bionic ball-end mill by combining different bionic structures with the BEM in order to improve the processing quality. Chang et al. [15] studied the mechanism of cutting aluminum alloy, gradually optimized the structure of the cutting tool through experiments, and finally accelerated the development of high-speed cutting tools, which reduced the development cost, optimized the tool design, and improved its performance. Liu et al. [16] optimized the R-angle edge shape of the conventional fillet-end milling cutter and designed a high-efficiency cutting tool with a large cutting depth that can effectively reduce the residual height of the machined workpiece surface. Guo et al. [17] designed a left-handed fillet-milling cutter that can process both the peripheral edge and the end edge at the same time, reducing the generation of burrs during machining. Zhao et al. [18] proposed a cutting tool design method combined with a cutting tool evaluation model for the BEM to obtain better surface performance. The experimental results showed that the tool designed using this method can maximize MRR on the premise of meeting the requirement of workpiece surface roughness. It is of great significance to improve the performance of parts. Through experiments, Bi et al. [19] proposed a multi-tooth milling cutter and analyzed the wear characteristics and processing performance in milling CFRP using the multi-tooth milling cutter. Masatoshi et al. [20] designed a new type of face milling cutter to realize an efficient, smooth surface and the high flutter stability machining of flexible thin plates. Li et al. [21] proposed a method that combined a variable pitch milling cutter with a damping effect, and designed a new type of vibration-resistant milling cutter using this method. Lee et al. [22] proposed the design model of the cutting edge and groove of a spherical taper milling cutter with equal pitch, which provided a theoretical basis for tool design. Denkena et al. [23] recently developed a new cutting tool grinding process for manufacturing cutting tools to deal with the high accuracy requirements of cutting tools. Yang et al. [24] effectively reduced the cutting temperature by placing micro-textures on the cutting tool surface, and put forward new ideas for cutting tool design. Wang et al. [25] proposed a cycloid milling cutter and verified that it can maintain good surface processing quality by using the cycloid milling cutter, showing excellent cutting performance. Antiago et al. [26] designed a semi-active magneto rheological damper for the chatter phenomenon generated during

the milling of thin-walled parts. Through experiments, it was verified that the damper had a good suppression effect on the chatter phenomenon of the cutting tool, thus improving the surface quality of the machined surface.

These scholars have made outstanding contributions to the design of cutting tools and high-quality processing. However, most of the tool innovations concern the design of micro-textures, cutting tool geometric parameters, and cutting tool processing methods, with few scholars committed to designing new cutting tools of high quality. This article aims to solve the existing processing problems by designing and manufacturing a DACT.

2. Design of DACT

2.1. Geometric Structure of DACT

The working surface of the DACT can be regarded as a surface of revolution; the axial longitudinal section profile of the DACT is shown in Figure 1. The profile surface of the end part of the DACT is composed of two tangent surfaces: a spherical surface at the bottom part of the cutting tool, and a ring torus, which is tangent to both the spherical surface and the cylinder part. Meanwhile, the axial longitudinal-section contour curve is composed of two tangent arcs L_e and L_r. The radius of the bottom spherical surface S_e is $SR_e = 3r$, the inner radius of the ring torus S_r is $R_r = r$, and the radius of the cylinder part of the DACT is $R_c = 2r$. The two tangent arcs L_e and L_r can be expressed as follows:

$$\begin{array}{l} L_e : \begin{cases} x = 3r\cos\theta_e \\ z = 3r\sin\theta_e - \sqrt{3}r \end{cases} \quad \left(\theta_e \in \left[\frac{\pi}{3}, \frac{\pi}{2}\right]\right) \\ \hline L_r : \begin{cases} x = r\cos\theta_r + r \\ z = r\sin\theta_r \end{cases} \quad \left(\theta_r \in \left[0, \frac{\pi}{3}\right]\right) \end{array} \tag{1}$$

where θ_e and θ_r are curve parameters.

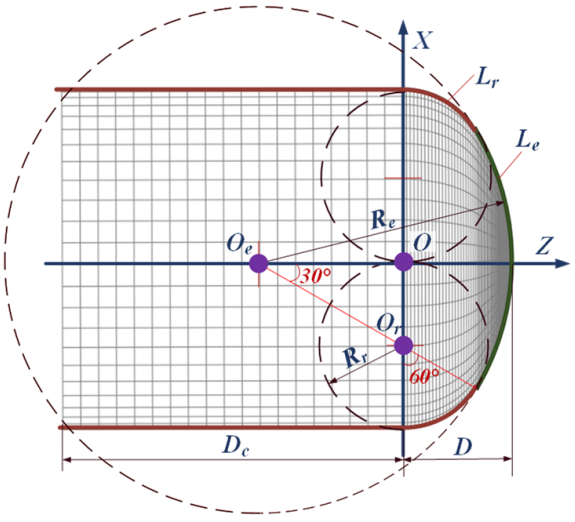


Figure 1. Geometric schematic diagram of the axial longitudinal section profile of DACT.

Then the ring torus surface S_r and the bottom spherical surface S_e can be defined as follows:

$$S_r = \{(r\cos\theta_r + r)\cos\varphi_r, (r\cos\theta_r + r)\sin\varphi_r, r\sin\theta_r\}\left(\theta_r \in \left[0, \frac{\pi}{3}\right], \varphi_r \in [0, 2\pi]\right) \tag{2}$$

$$S_e = \left\{3r\cos\theta_e\cos\varphi_e, 3r\cos\theta_e\sin\varphi_e, 3r\sin\theta_e - \sqrt{3}r\right\}\left(\theta_e \in \left[\frac{\pi}{3}, \frac{\pi}{2}\right], \varphi_e \in [0, 2\pi]\right) \tag{3}$$

where φ_e and φ_r are surface parameters.

It is easy to obtain the cylindrical surface S_c as follows:

$$S_c = \{2r\cos\varphi_c, 2r\sin\varphi_c, u\}(u \in [-D_c, 0], \varphi_c \in [0, 2\pi]) \quad (4)$$

where D_c is the axial length of the circumferential cutting edge.

2.2. Cutting Geometry Model of DACT

When a BEM is used for machining a small curvature surface, the radius of the cutting tool limits the processing quality. In the case of the same cutting parameters as the BEM, the DACT can obtain a wider cutting width and better processing quality.

2.2.1. Comparison of Effective Cutting Speed between DACT and BEM

As shown in Figure 2, the radius of both the DACT and BEM is $2r$, the tilt angle of the inclined plane is $\alpha(\alpha \in [0,\pi/2])$, and the rotational speed of the cutting tools is n. Thus, the effective cutting speed V_B of the BEM can be expressed as follows, according to the geometric relationship shown in Figure 2:

$$V_B = 4r\pi n\sin\alpha \quad (5)$$

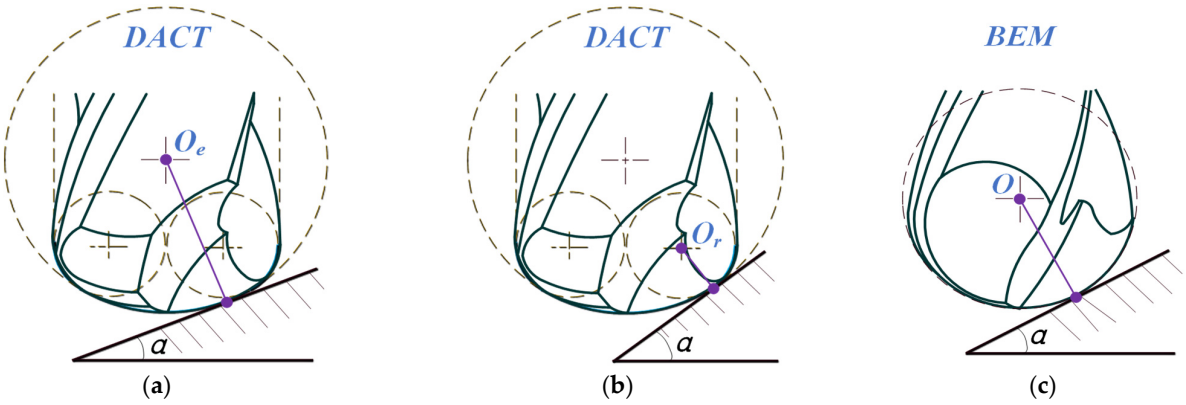


Figure 2. Schematic diagram of cutting process: (**a**) cutting contact point located on the bottom arc L_e of DACT; (**b**) cutting contact point located on the ring arc L_r of DACT; (**c**) cutting contact point located on circular arc of BEM.

When the cutting contact point is located on the bottom arc L_e of the DACT, the effective cutting speed V_e of the DACT can be defined as follows:

$$V_e = 6r\pi n\sin\alpha \quad (6)$$

When the cutting contact point is located on the ring arc L_r of the DACT, the effective cutting speed V_r of the DACT can be defined as follows:

$$V_r = 2\pi rn(1+\sin\alpha) \quad (7)$$

According to the above cutting speed formulas, the cutting speed comparison between the BEM and DACT is shown in Figure 3. The radius of the BEM and DACT is 5 mm, parameter r is 2.5 mm, and the rotational speed of the cutting tool n is 2500 r/min.

Figure 3 shows that the effective cutting speed will increase with the tilt angle α, and the effective cutting speed of the DACT is always larger than that of the BEM. When the cutting contact point is located on the tangent point of the double arcs (L_e and L_r) and the tilt angle α is $\pi/6$, the difference in the effective cutting speeds between the DACT and BEM is the largest.

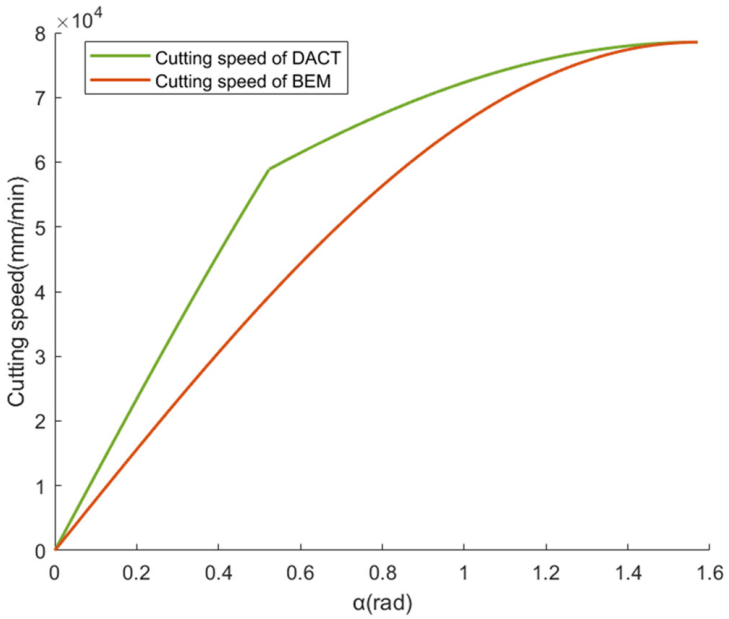


Figure 3. Comparison of effective cutting speeds.

2.2.2. Cutting Residual Height of DACT

The geometric contact relationship between the cutting tool and the workpiece surface when machining the workpiece is shown in Figure 4. The tool coordinate system is O-XYZ; in the local region of the current cutting contact point O', the design surface is approximated as the tangent plane X'-O'-Y' at the current cutting contact point O'. Meanwhile, the workpiece surface X_w-O_w-Y_w is approximated as the parallel plane of X'-O'-Y', and the inclination angle of the tangent plane X'-O'-Y' is denoted as α. According to the geometric structure of the DACT, when $\alpha \in [0,\pi/6]$, the cutting contact point O' is located on the bottom arc L_e of the DACT, and then O' can be expressed as $\{3r\sin\alpha, 0, 3r\cos\alpha - \sqrt{3}r\}$; when $\alpha \in [\pi/6,\pi/2]$, the cutting contact point O' is located on the ring arc L_r of the DACT, and then O' can be expressed as $\{r\sin\alpha+r, 0, r\cos\alpha\}$.

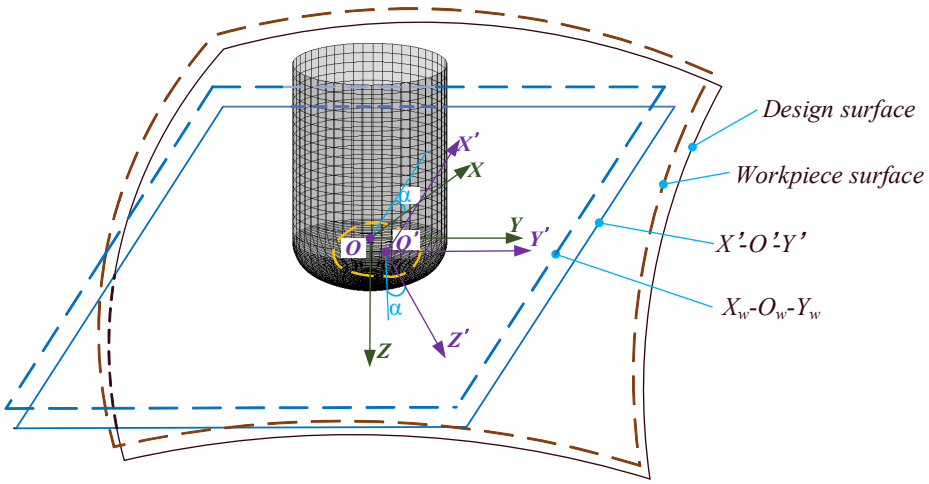


Figure 4. Geometric contact relationship.

As shown in Figure 5, the inclination angle α, cutting depth a_p, and tool geometry parameter r jointly determine which part of the cutting tool actually participates in the cutting process. Therefore, the cutting modes of the DACT can be divided into six cases.

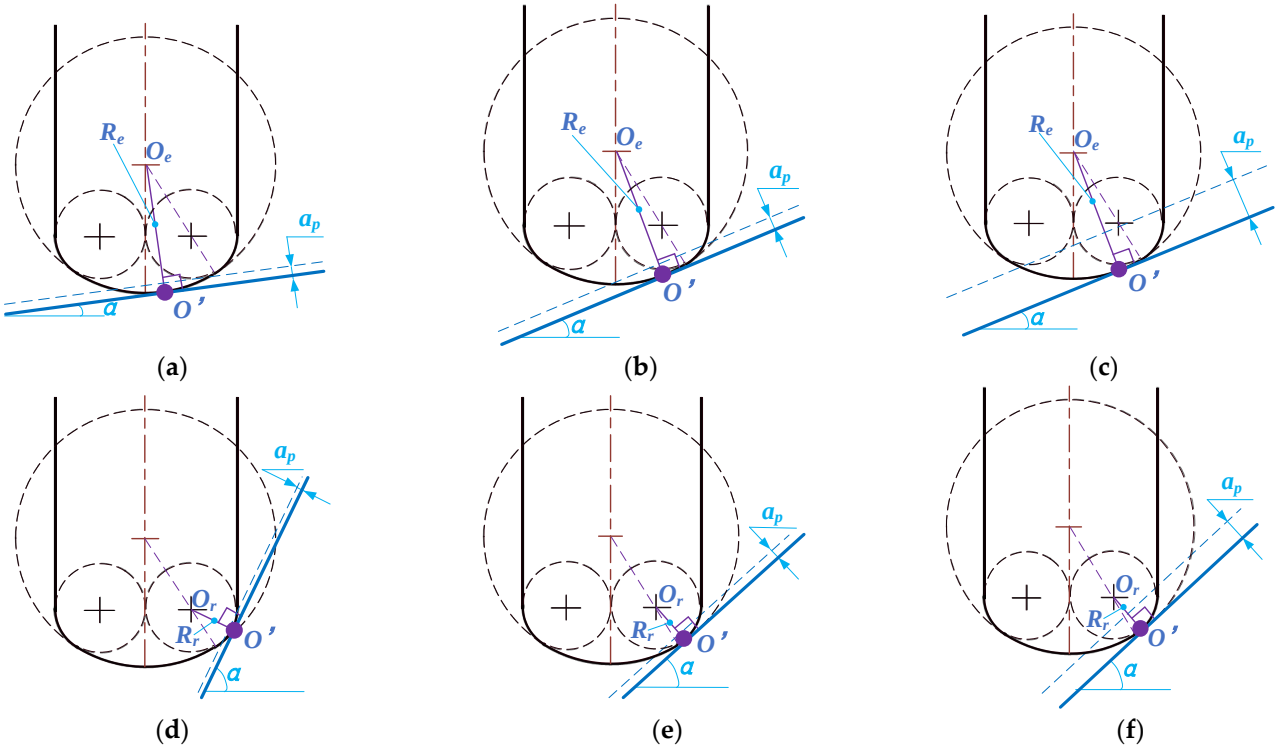


Figure 5. Schematic diagrams of cutting modes of DACT: (**a**) O' is located on L_e, and only L_e is involved in cutting; (**b**) O' is located on L_e, and L_e and L_r participate in cutting; (**c**) O' is located on L_e, and L_e, L_r, and the peripheral cutting edge participate in cutting simultaneously; (**d**) O' is located on L_r, and only L_r is involved in cutting; (**e**) O' is located on L_r, and L_r and the peripheral cutting edge participate in cutting; (**f**) O' is located on L_r, and L_e, L_r, and the peripheral cutting edge participate in cutting simultaneously.

When $\alpha \in [0,\pi/6 - \arccos(1 - a_p/3r)]$, only the bottom arc L_e is involved in cutting, as shown in area ① in Figure 6.

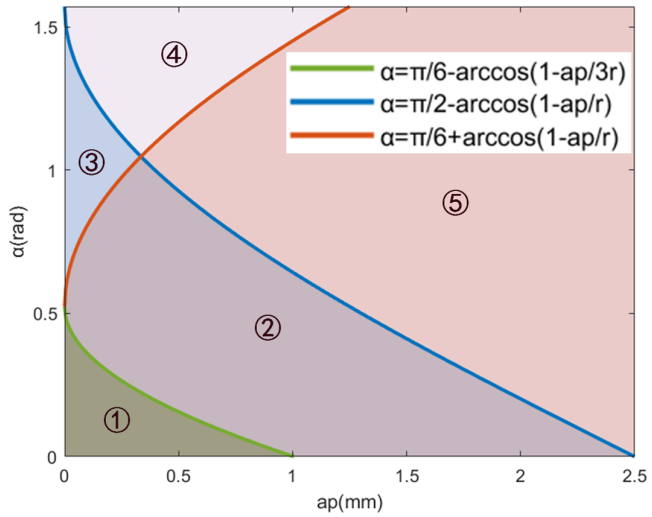


Figure 6. Relationship between cutting mode, inclination angle α, cutting depth a_p, and tool parameter r.

When $\alpha \in [\pi/6 - \arccos(1 - a_p/3r), \pi/6 + \arccos(1 - a_p/r)]$ $(a_p \in [0,r - \sqrt{3}r/2]) \cup \alpha \in [\pi/6 - \arccos(1 - a_p/3r),\pi/2 - \arccos(1 - a_p/r)]$ $(a_p \in [r - \sqrt{3}r/2,r])$, the bottom arc L_e and ring arc L_r are involved in cutting, as shown in area ② in Figure 6.

When $\alpha \in [\pi/6 + \arccos(1 - a_p/r), \pi/2 - \arccos(1 - a_p/r)]$ ($a_p \in [0, r - \sqrt{3}r/2]$), only the ring arc L_r is involved in cutting, as shown in area ③ in Figure 6.

When $\alpha \in [\pi/2 - \arccos(1 - a_p/r), \pi/2]$ ($a_p \in [0, r - \sqrt{3}r/2]$) $\cup$ $\alpha \in [\pi/6 + \arccos(1 - a_p/r), \pi/2]$ ($a_p \in [r - \sqrt{3}r/2, r]$), the ring arc L_r and peripheral cutting edge of the DACT are involved in cutting simultaneously, as shown in area ④ in Figure 6.

When $\alpha \in [\pi/2 - \arccos(1 - a_p/r), \pi/6 + \arccos(1 - a_p/r)]$ ($a_p \in [r - \sqrt{3}r/2, r]$), the bottom arc L_e, ring arc L_r, and peripheral cutting edge participate in cutting, as shown in area ⑤ in Figure 6.

The section curve of the cutting tool in the plane X_w-O_w-Y_w is the intersection curve of the cutting tool and workpiece surface. The intersection curve is a closed curve, which determines the effective cutting width in the cutting process.

Translate the origin O (0,0,0) of the tool coordinate system O-XYZ to the cutting contact point O', and rotate the OX and OZ axes with angle α counterclockwise around the OY axis simultaneously. Through the above two transformations, the local coordinate system O'-$X'Y'Z'$ can be obtained.

When the cutting contact point O' is $\{C_1,0,C_2\}$, thus, when $\alpha \in [0,\pi/6]$, $C_1 = 3r\sin\alpha$, $C_2 = 3r\cos\alpha - \sqrt{3}r$; when $\alpha \in [\pi/6,\pi/2]$, $C_1 = r\sin\alpha + r$, $C_2 = r\cos\alpha$.

The cutting tool rotation surface in coordinate system O'-$X'Y'Z'$ can be expressed as follows:

$$\begin{bmatrix} x' \\ y' \\ z' \end{bmatrix} = \begin{bmatrix} \cos\alpha & 0 & -\sin\alpha \\ 0 & 1 & 0 \\ \sin\alpha & 0 & \cos\alpha \end{bmatrix} \begin{bmatrix} x - C_1 \\ y \\ z - C_2 \end{bmatrix} \tag{8}$$

Make $z' = a_p$, and then the general expression of the intersection curves of the cutting tool and plane X_w-O_w-Y_w can be obtained as follows:

$$\begin{bmatrix} (C_2 - G(\theta))\csc\alpha + a_p\cot\alpha \\ \pm\sqrt{F^2(\theta) - \left((C_2 - G(\theta))\cot\alpha + a_p\csc\alpha + C_1\right)^2} \\ a_p \end{bmatrix} \tag{9}$$

where $\begin{cases} F_e(\theta) = 3r\cos\theta_e \\ G_e(\theta) = 3r\sin\theta_e - \sqrt{3}r \end{cases}$ $\left(\theta_e \in \left[\frac{\pi}{3}, \frac{\pi}{2}\right]\right)$; $\begin{cases} F_r(\theta) = r\cos\theta_r + r \\ G_r(\theta) = r\sin\theta_r \end{cases}$ $\left(\theta_r \in \left[0, \frac{\pi}{3}\right]\right)$.

As shown in Figure 7, the green curve is the intersection curve of the bottom spherical surface of the DACT and the workpiece surface; the red curve is the intersection curve of the ring torus of the DACT and the workpiece surface; and the blue curve is the intersection curve of the cylindrical part of the DACT and the workpiece surface.

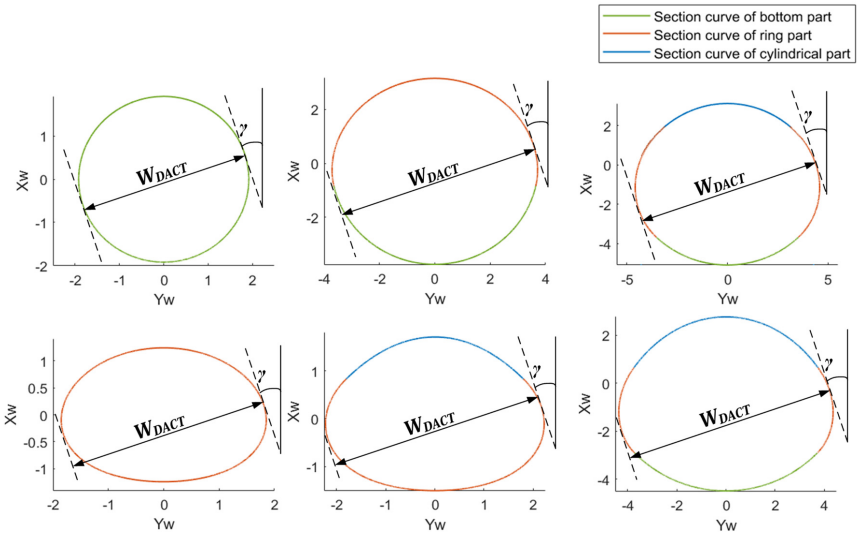


Figure 7. Intersection curves in plane X_w-O_w-Y_w.

The included angle γ between the feed direction of the cutting tool and the X_w axis, the geometric parameter r, the inclination angle α, and the cutting depth a_p are the main factors that affect the effective cutting width of the DACT, as shown in Figure 7.

When only the bottom spherical part is involved in the cutting, the effective cutting width of the DACT is:

$$W_{DACT} = 2\sqrt{6ra_p - {a_p}^2} \tag{10}$$

When cutting with a BEM, the intersection curve between the cutting tool and the workpiece is approximately circular. Thus, the effective cutting width of the BEM can be obtained as follows:

$$W_{BEM} = 2\sqrt{2Ra_p - {a_p}^2} \tag{11}$$

Above all, the effective cutting width of the DACT is larger than that of the BEM by selecting an appropriate feed direction angle γ so that more materials can be removed.

When the feed direction angle γ is 0, the cutting width of the DACT is the largest. When $\gamma = 0$, the normal section at the current cutting contact point O' is Y'-O'-Z'. Then, the general expression of the intersection curves of the cutting tool and plane Y'-O'-Z' can be obtained as follows:

$$\begin{bmatrix} 0 \\ \pm\sqrt{F^2(\theta) - ((G(\theta) - C_2)\tan\alpha + C_1)^2} \\ (G(\theta) - C_2)\sec\alpha \end{bmatrix} \tag{12}$$

where $\begin{cases} F_e(\theta) = 3r\cos\theta_e \\ G_e(\theta) = 3r\sin\theta_e - \sqrt{3}r \end{cases} \left(\theta_e \in \left[\frac{\pi}{3}, \frac{\pi}{2}\right]\right); \begin{cases} F_r(\theta) = r\cos\theta_r + r \\ G_r(\theta) = r\sin\theta_r \end{cases} \left(\theta_r \in \left[0, \frac{\pi}{3}\right]\right)$.

The intersection curves of the DACT in the normal section Y'-O'-Z' are shown in Figure 8.

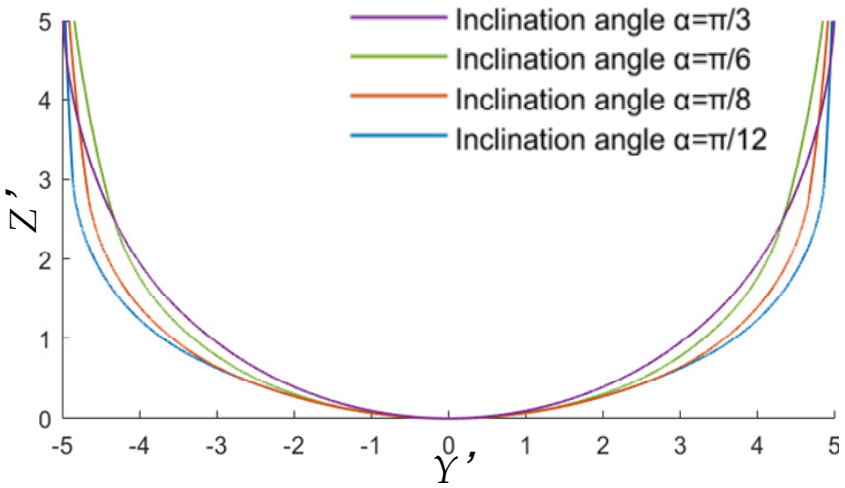


Figure 8. Intersection curves of DACT and normal section Y'-O'-Z'.

Therefore, when the tool path interval is L, the intersection curves of the cutting tools in Y'-O'-Z' determines the cutting scallop height, as shown in Figure 9.

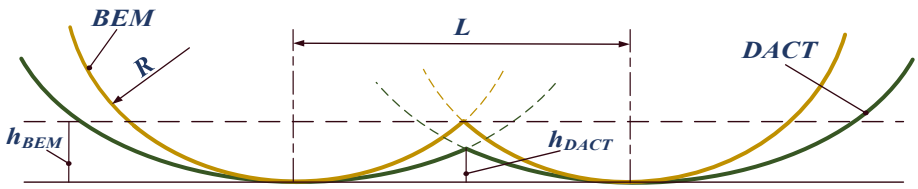


Figure 9. Comparison schematic diagram of cutting scallop height.

When $\alpha \in [0,\pi/6]$, $L \leq \sqrt{9r^2 - 27r^2\tan^2\alpha}$, the cutting scallop height h_{ee} of the DACT is:

$$h_{ee} = \frac{6r - \sqrt{36r^2 - L^2}}{2} \tag{13}$$

When $\alpha \in [0,\pi/6]$, $\sqrt{9r^2 - 27r^2\tan^2\alpha} \leq L \leq \sqrt{16r^2 - 12r^2\tan^2\alpha}$, the cutting scallop height h_{er} of the DACT is:

$$h_{er} = 3r - r\sec\alpha\left(\sin\theta + \sqrt{3}\right) \tag{14}$$

where $\sqrt{9r^2 - 27r^2\tan^2\alpha} \leq L \leq \sqrt{16r^2 - 12r^2\tan^2\alpha}$.

When $\alpha \in [0,\pi/6]$, $\sqrt{16r^2 - 12r^2\tan^2\alpha} \leq L \leq 4r$, the cutting scallop height h_{er} of the DACT is:

$$h_{er} = 3r - \frac{\csc\alpha\sqrt{16r^2 - L^2}}{2} \tag{15}$$

When $\alpha \in [\pi/6, \pi/2]$, $L \leq 2\sqrt{3}\,r$, the cutting scallop height h_{rr} of the DACT is:

$$h_{rr} = r - r\sec\alpha\sin\theta \tag{16}$$

where $4r^2(\cos\theta + 1)^2 - 4r^2(\sin\theta\tan\alpha + 1)^2 - L^2 = 0$.

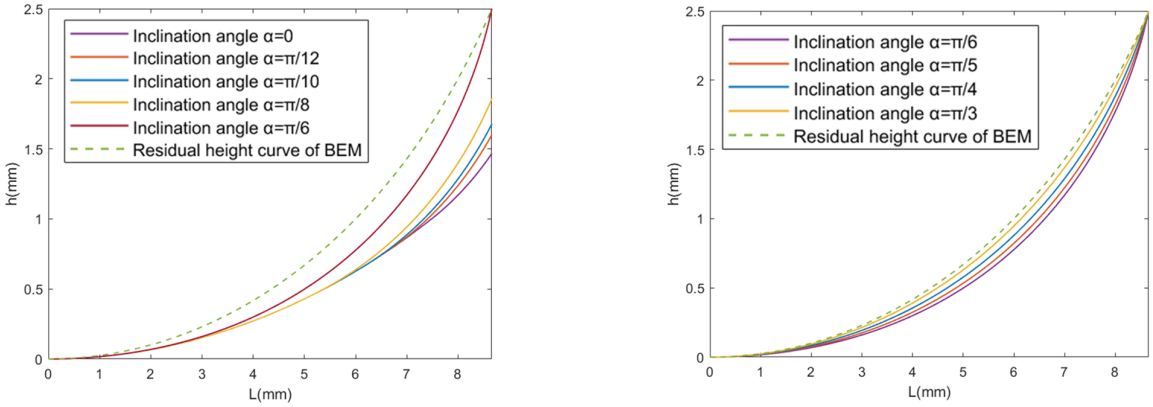
When $\alpha \in [\pi/6, \pi/2]$, $2\sqrt{3}\,r \leq L \leq 4\,r$, the cutting scallop height h_{rc} of the DACT is:

$$h_{rc} = r(1 + \csc\alpha) - \frac{\csc\alpha\sqrt{16r^2 - L^2}}{2} \tag{17}$$

The cutting scallop height h_{BEM} of the BEM is:

$$h_{BEM} = R - \frac{\sqrt{4R^2 - L^2}}{2} \tag{18}$$

When $\alpha \in [0,\pi/6]$, the cutting contact point O' of the DACT is located on the bottom arc; the relationship between the cutting scallop height h and the tool path interval L is shown in Figure 10a. The radius of the DACT and BEM is 5 mm, as shown in Figure 10.



(**a**) (**b**)

Figure 10. Relationship between L and h: (**a**) cutting contact point O' is located on the bottom arc; (**b**) cutting contact point O' is located on the ring arc.

When $\alpha \in [\pi/6, \pi/2]$, the cutting contact point O' of the DACT is located on the ring arc. Figure 10b shows the relationship between the cutting scallop height h and the tool path interval L at this time.

The dotted line in Figure 10 is the cutting scallop height curve of the BEM. As shown in Figure 10, the cutting scallop height of the DACT is always smaller than that of the

BEM. Meanwhile, the smaller the α, the greater the difference between the BEM and DACT. Therefore, the DACT is more suitable for machining surfaces with a small curvature. With the same cutting depth, the residual height of the DACT is smaller than the BEM, and therefore the processing quality will be better.

2.3. Cutting Edge Design and Numerical Simulation of DACT

2.3.1. Cutting Edge with Constant Helix Angle of DACT

The general mathematical model of the cutting edge with a constant helix angle is shown as follows:

$$\begin{cases} \{F(\theta)\cos\varphi, F(\theta)\sin\varphi, G(\theta)\} \\ \varphi = \tan\beta \int_{\theta_0}^{\theta} \frac{\sqrt{F'^2(\theta)+G'^2(\theta)}}{F(\theta)} \mathrm{d}\theta \end{cases} \tag{19}$$

where β is the helix angle of cutting edge.

According to the mathematical models of the bottom spherical surface in Equation (3), the following formulas can be obtained as follows:

$$F_e(\theta) = 3r\cos\theta, G_e(\theta) = 3r\sin\theta - \sqrt{3}r \tag{20}$$

$$F'_e(\theta) = -3r\sin\theta, G'_e(\theta) = 3r\cos\theta \tag{21}$$

Based on the principles of differential geometry, by integrating Equations (19)–(21), parameter $\varphi_{\beta e}$ can be calculated as follows:

$$\varphi_{\beta e} = \tan\beta\left[\ln\tan\left(\frac{\pi}{4}+\frac{\theta}{2}\right)\right] + \varphi_{\beta e0} \tag{22}$$

According to the mathematical models of the ring torus surface in Equation (2), the following formulas can be obtained as follows:

$$F_r(\theta) = r\cos\theta + r, G_r(\theta) = r\sin\theta \tag{23}$$

$$F'_r(\theta) = -r\sin\theta, G'_r(\theta) = r\cos\theta \tag{24}$$

Based on the principles of differential geometry, by integrating Equations (19), (23), and (24), parameter $\varphi_{\beta r}$ can be calculated as follows:

$$\varphi_{\beta r} = \tan\beta\tan\frac{\theta}{2} + \varphi_{\beta r0} \tag{25}$$

According to the mathematical models of the cylindrical surface in Equation (4), the following formulas can be obtained as follows:

$$F_c(u) = 2r, G_c(u) = u \tag{26}$$

$$F'_c(u) = 0, G'_c(u) = 1 \tag{27}$$

Based on the principles of differential geometry, by integrating Equations (19), (26), and (27), parameter $\varphi_{\beta c}$ can be calculated as follows:

$$\varphi_{\beta c} = \frac{u\tan\beta}{2r} + \varphi_{\beta c0} \tag{28}$$

Considering the smooth transition of the cutting edge with a constant helix angle on the bottom spherical surface, the ring torus surface, and the cylindrical surface:

Set when $\theta = 0$, $\varphi_{\beta r} = \varphi_{\beta c} = 0$, and then $\varphi_{\beta r0} = \varphi_{\beta c0} = 0$.

Set when $\theta = \frac{\pi}{3}$, $\varphi_{\beta e} = \varphi_{\beta r}$ and then $\varphi_{\beta e0} = \tan\beta\left[\frac{\sqrt{3}}{3} - \ln(2+\sqrt{3})\right]$.

According to the principle of differential geometry, the solution of parameters $\varphi_{\beta r}$, $\varphi_{\beta e}$, and $\varphi_{\beta c}$ can be introduced into Equations (2)–(4), respectively. Then, the cutting edge with a constant helix angle of the DACT can be obtained as follows:

$$\begin{cases} R_{\beta r} = \{(r\cos\theta + r)\cos\varphi_{\beta r}, (r\cos\theta + r)\sin\varphi_{\beta r}, r\sin\theta\} \\ \varphi_{\beta r} = \tan\beta\left[\ln\tan\left(\frac{\pi}{4} + \frac{\theta}{2}\right)\right] + \tan\beta\left[\frac{\sqrt{3}}{3} - \ln(2+\sqrt{3})\right] \end{cases} \left(\theta \in \left[0, \tfrac{\pi}{3}\right]\right)$$
$$\begin{cases} R_{\beta e} = \left\{3r\cos\theta\cos\varphi_{\beta e}, 3r\cos\theta\sin\varphi_{\beta e}, 3r\sin\theta - \sqrt{3}r\right\} \\ \varphi_{\beta e} = \tan\beta\tan\frac{\theta}{2} \end{cases} \left(\theta \in \left[\tfrac{\pi}{3}, \tfrac{\pi}{2}\right]\right) \quad (29)$$
$$\begin{cases} R_{\beta c} = \left\{2r\cos\varphi_{\beta c}, 2r\sin\varphi_{\beta c}, u\right\} \\ \varphi_{\beta c} = \frac{u\tan\beta}{2r} \end{cases} (u \in [-D_C, 0])$$

2.3.2. Cutting Edge with Constant Pitch of DACT

The general mathematical model of cutting edge with constant pitch is shown as follows:

$$\begin{cases} \{F(\theta)\cos\varphi, F(\theta)\sin\varphi, G(\theta)\} \\ \varphi = \frac{1}{b}\int_{\theta_0}^{\theta}\sqrt{F'^2(\theta) + G'^2(\theta)}d\theta \end{cases} \quad (30)$$

where b is the helical parameter.

$$b = \frac{2r}{\tan\beta_0} \quad (31)$$

where β_0 is the helix angle of the cutting edge at the cylindrical part of the DACT.

Based on the principles of differential geometry, by integrating Equations (20), (21), and (30), parameter φ_{be} can be calculated as follows:

$$\varphi_{be} = \frac{3r\theta}{b} + \varphi_{be0} \quad (32)$$

Based on the principles of differential geometry, by integrating Equations (23), (24), and (30), parameter φ_{br} can be calculated as follows:

$$\varphi_{br} = \frac{r\theta}{b} + \varphi_{br0} \quad (33)$$

Based on the principles of differential geometry, by integrating Equations (26), (27), and (30), parameter φ_{bc} can be calculated as follows:

$$\varphi_{bc} = \frac{u}{b} + \varphi_{bc0} \quad (34)$$

Considering the smooth transition of the cutting edge with constant pitch on the bottom spherical surface, the ring torus and the cylindrical surface:

Set when $\theta = 0$, $\varphi_{br} = \varphi_{bc} = 0$, and then $\varphi_{br0} = \varphi_{bc0} = 0$;

Set when $\theta = \frac{\pi}{3}$, $\varphi_{be} = \varphi_{br}$, and then $\varphi_{be0} = -\frac{2r\pi}{3b}$.

According to the principle of differential geometry, the solution of parameters φ_{br}, φ_{be}, and φ_{bc} can be introduced into Equations (2)–(4), respectively. Then, the cutting edge with the constant pitch of the DACT can be obtained as follows:

$$\begin{cases} R_{br} = \{(r\cos\theta + r)\cos\varphi_{br}, (r\cos\theta + r)\sin\varphi_{br}, r\sin\theta\} \\ \varphi_{br} = \frac{r\theta}{b} \end{cases} \left(\theta \in \left[0, \tfrac{\pi}{3}\right]\right)$$
$$\begin{cases} R_{be} = \left\{3r\cos\theta\cos\varphi_{be}, 3r\cos\theta\sin\varphi_{be}, 3r\sin\theta - \sqrt{3}r\right\} \\ \varphi_{be} = \frac{3r\theta}{b} - \frac{2r\pi}{3b} \end{cases} \left(\theta \in \left[\tfrac{\pi}{3}, \tfrac{\pi}{2}\right]\right) \quad (35)$$
$$\begin{cases} R_{bc} = \{2r\cos\varphi_{bc}, 2r\sin\varphi_{bc}, u\} \\ \varphi_{bc} = \frac{u}{b} \end{cases} (u \in [-D_c, 0])$$

2.3.3. Orthogonal Spiral Cutting Edge of The DACT

The cutting edge can also be obtained as the intersecting curve when the orthogonal helical surface intersects with the milling cutter's working surface.

The orthogonal helical surface can be expressed as follows:

$$S_o = \{R_z \cos\varphi, R_z sin\varphi, P_z\varphi/2\pi\}(0 \le R_z \le R) \tag{36}$$

where P_z is the helical pitch and R_z is the radius of a selected point on the orthogonal helical surface.

$$\frac{P_z}{2\pi R} = \frac{1}{\tan\beta_0} \tag{37}$$

where β_0 is the helix angle of the cutting edge at the cylindrical part of the DACT.

By combining Equations (2)–(4), (36), and (37), parameters φ_{or}, φ_{oe}, and φ_{oc} can be deduced as follows:

$$\varphi_{or} = \frac{\sin\theta\tan\beta_0}{2} \tag{38}$$

$$\varphi_{oe} = \frac{\left(3r\sin\theta - \sqrt{3}r\right)\tan\beta_0}{2r} \tag{39}$$

$$\varphi_{oc} = \frac{u\tan\beta_0}{2r} \tag{40}$$

The solution of parameters φ_{or}, φ_{oe}, and φ_{occ} can be introduced into Equations (2)–(4), respectively, and then the orthogonal spiral cutting edge of the DACT can be obtained as follows:

$$\begin{cases} R_{or} = \{(r\cos\theta + r)\cos\varphi_{or}, (r\cos\theta + r)\sin\varphi_{or}, r\sin\theta\} & \left(\theta \in \left[0, \frac{\pi}{3}\right]\right) \\ \varphi_{or} = \frac{\sin\theta\tan\beta_0}{2} & \\ R_{oe} = \left\{3r\cos\theta\cos\varphi_{oe}, 3r\cos\theta\sin\varphi_{oe}, 3r\sin\theta - \sqrt{3}r\right\} & \left(\theta \in \left[\frac{\pi}{3}, \frac{\pi}{2}\right]\right) \\ \varphi_{oe} = \frac{\left(3r\sin\theta - \sqrt{3}r\right)\tan\beta_0}{2r} & \\ \begin{cases} R_{oc} = \{2r\cos\varphi_{oc}, 2r\sin\varphi_{oc}, u\} & (u \in [-D_c, 0]) \\ \varphi_{oc} = \frac{u\tan\beta_0}{2r} & \end{cases} & \end{cases} \tag{41}$$

The three continuous edge curve models of the DACT established above are summarized in Table 1.

Table 1. Three types of cutting edge curves of DACT.

Different Cutting Edge Types	R	φ
Cutting edge with constant helix angle	$\left\{3r\cos\theta\cos\varphi_{\beta e}, 3r\cos\theta\sin\varphi_{\beta e}, 3r\sin\theta - \sqrt{3}r\right\}$ $\left(\theta \in \left[\frac{\pi}{3}, \frac{\pi}{2}\right]\right)$ $\{(r\cos\theta + r)\cos\varphi_{\beta r}, (r\cos\theta + r)\sin\varphi_{\beta r}, r\sin\theta\}$ $\left(\theta \in \left[0, \frac{\pi}{3}\right]\right)$ $\{2r\cos\varphi_{\beta c}, 2r\sin\varphi_{\beta c}, u\}$ $(u \in [-D_c, 0])$	$\tan\beta\tan\frac{\theta}{2}$ $\varphi_{\beta r} = \tan\beta\left[\ln\tan\left(\frac{\pi}{4} + \frac{\theta}{2}\right)\right] + \tan\beta\left[\frac{\sqrt{3}}{3} - \ln(2 + \sqrt{3})\right]$ $\varphi_{\beta c} = \frac{u\tan\beta}{2r}$
Cutting edge with constant pitch	$\left\{3r\cos\theta\cos\varphi_{be}, 3r\cos\theta\sin\varphi_{be}, 3r\sin\theta - \sqrt{3}r\right\}$ $\left(\theta \in \left[\frac{\pi}{3}, \frac{\pi}{2}\right]\right)$ $\{(r\cos\theta + r)\cos\varphi_{br}, (r\cos\theta + r)\sin\varphi_{br}, r\sin\theta\}\left(\theta \in \left[0, \frac{\pi}{3}\right]\right)$ $\{2r\cos\varphi_{bc}, 2r\sin\varphi_{bc}, u\}$ $(u \in [-D_c, 0])$	$\varphi_{be} = \frac{3r\theta}{b} - \frac{2r\pi}{3b}$ $\varphi_{br} = \frac{r\theta}{b}$ $\varphi_{bc} = \frac{u}{b}$
Orthogonal spiral cutting edge	$\left\{3r\cos\theta\cos\varphi_{oe}, 3r\cos\theta\sin\varphi_{oe}, 3r\sin\theta - \sqrt{3}r\right\}$ $\left(\theta \in \left[\frac{\pi}{3}, \frac{\pi}{2}\right]\right)$ $\{(r\cos\theta + r)\cos\varphi_{or}, (r\cos\theta + r)\sin\varphi_{or}, r\sin\theta\}\left(\theta \in \left[0, \frac{\pi}{3}\right]\right)$ $\{2r\cos\varphi_{oc}, 2r\sin\varphi_{oc}, u\}$ $(u \in [-D_c, 0])$	$\varphi_{oe} = \frac{\left(3r\sin\theta - \sqrt{3}r\right)\tan\beta_0}{2r}$ $\varphi_{or} = \frac{\sin\theta\tan\beta_0}{2}$ $\varphi_{oc} = \frac{u\tan\beta_0}{2r}$

2.3.4. Numerical Simulations of Cutting Edge Curves of DACT

Based on the mathematical models proposed in this paper, numerical simulation is carried out for all of these cutting edge curves. The numerical simulations of the tool rotation surface, cutting edge with a constant helix angle, cutting edge with a constant pitch, and the orthogonal spiral cutting edge are carried out based on MATLAB. Take a DACT with two grooves as an example for convenience. The simulation results are shown in Figure 11 where the radius of the DACT is 5 mm and the helix angle of the cutting edge at the cylindrical part is $\pi/6$.

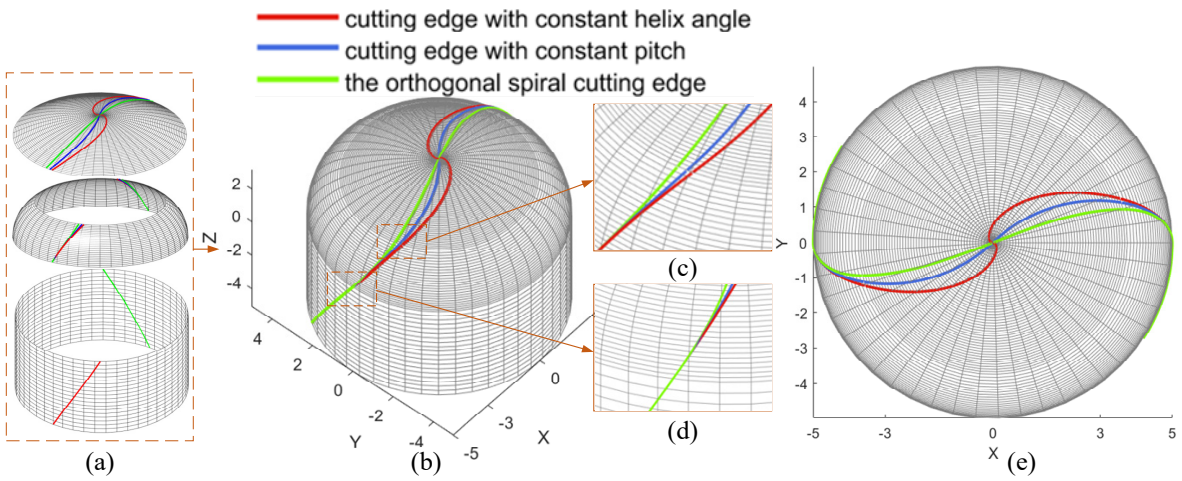


Figure 11. Simulation of three types of cutting edge curves of DACT: (**a**) three parts of DACT; (**b**) three types of cutting edge curves of DACT; (**c**) enlarged view of the transition area between the cutting edge of the bottom part and the ring torus part; (**d**) enlarged view of the transition area between the cutting edge of the ring torus part and the cylindrical part; (**e**) top view of cutting edge curves.

3. Fabrications and Detection of DACT

The DACT and BEM with a constant pitch cutting edge are manufactured as an example in the five-axis tool grinding center manufactured by Saacke, as shown in Figure 12.

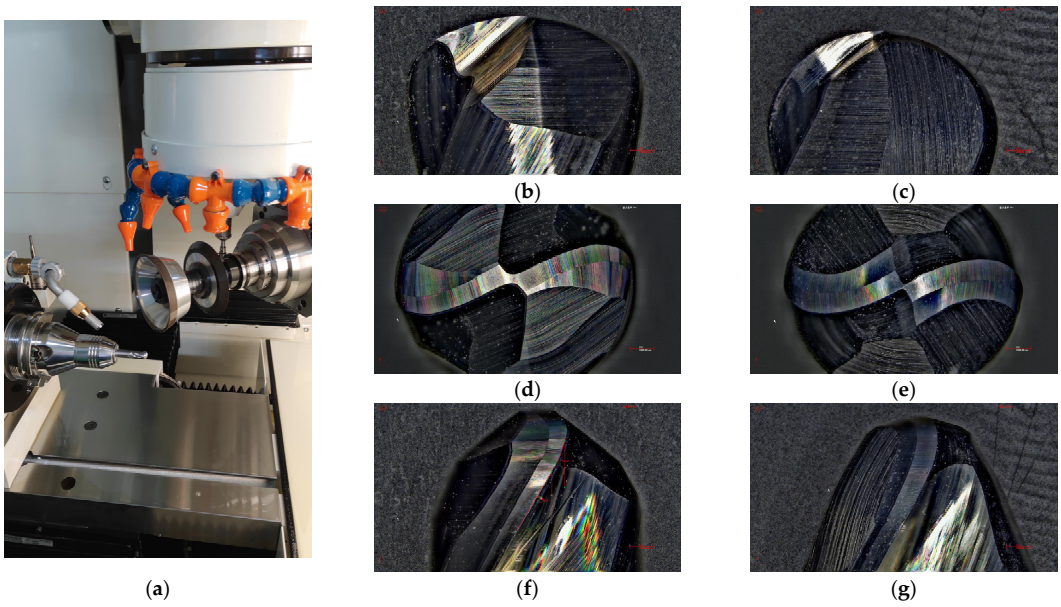
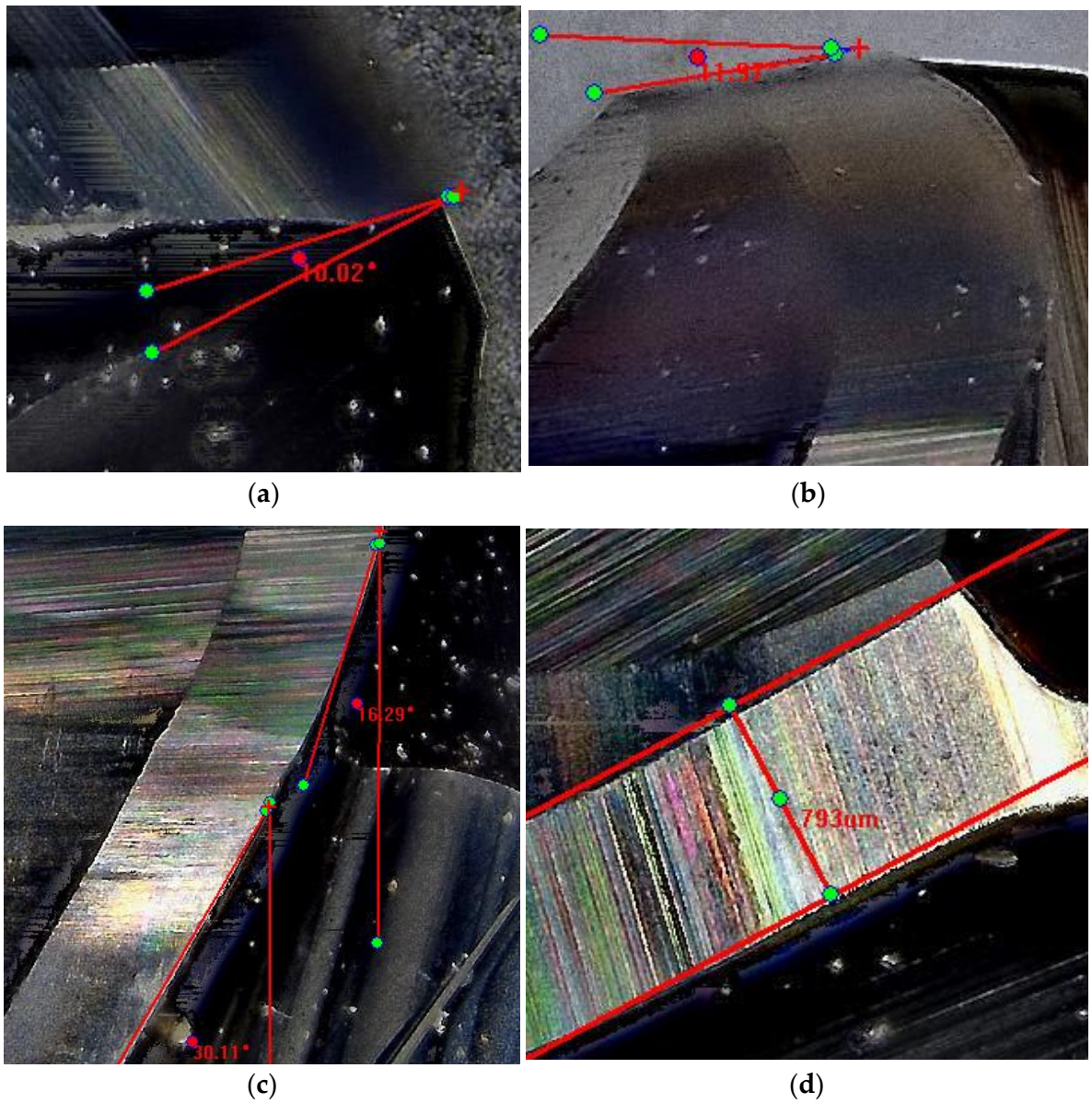


Figure 12. Grinding site and cutting tools: (**a**) grinding site of DACT and BEM; (**b**) front view of DACT; (**c**) front view of BEM; (**d**) top view of DACT; (**e**) top view of BEM; (**f**) side view of DACT; (**g**) side view of BEM.

To ensure the accuracy of the experimental data, the manufacturing accuracy index of the cutting tools are selected as follows: the length of the end teeth should be ± 0.005 mm, the flank face width should be ± 0.008 mm, the helix angle should be $\pm 0.15^{\circ}$, the relief angle should be $\pm 0.05^{\circ}$, and the rake angle should be $\pm 0.05^{\circ}$. The radius of the cutting tool should be 10 mm, the spiral angle should be $\pi/6$, the rake angle should be 10°, the relief angle should be 12°, and the flank face width should be 0.8 mm.

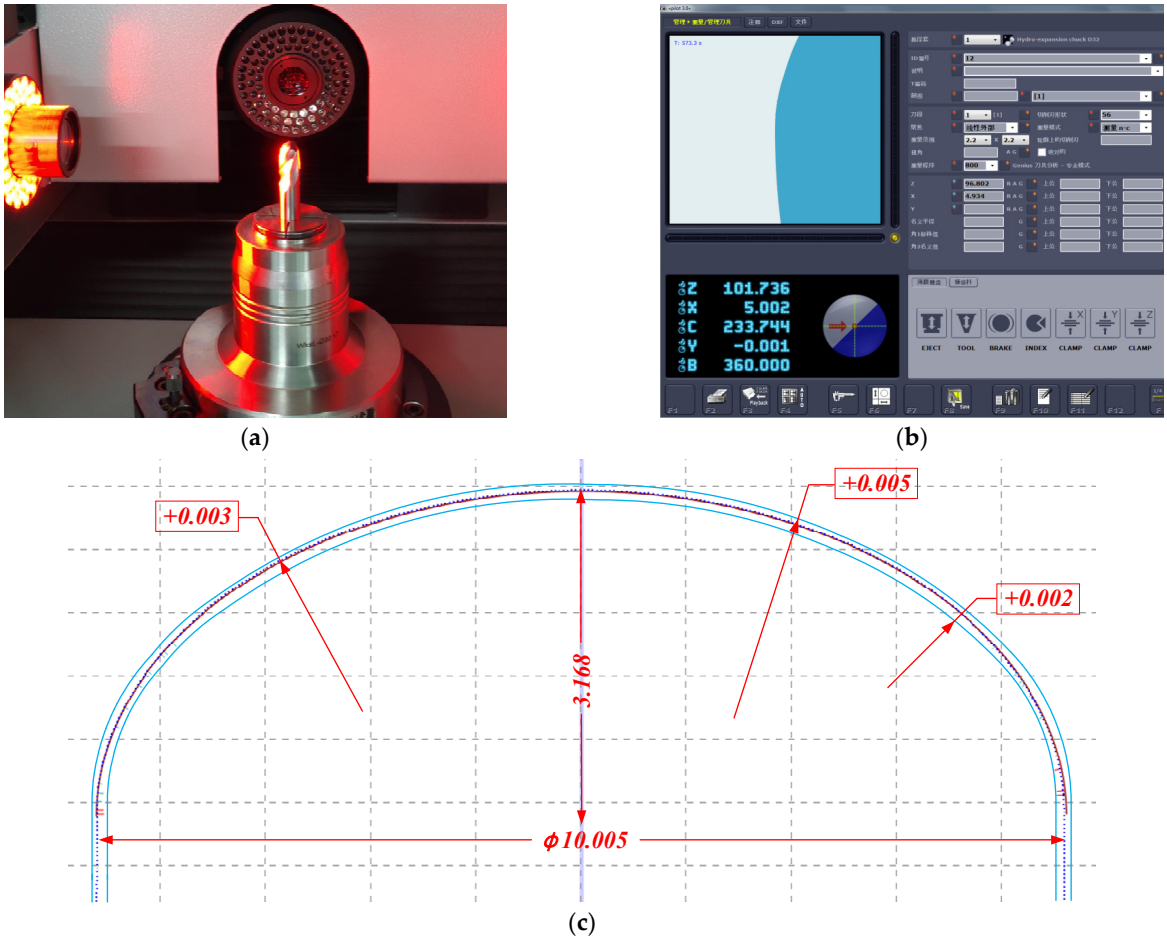
A PZ-CS3500A 3D microscope system with super depth of field was adopted to measure the geometric parameters of the double-arc milling cutter DACT, and the measurement results are shown in Figure 13. And the Zoller G3 tool test center was applied in the tool geometric measurement as shown in Figure 14. As shown in Figure 13, the rake angle and the relief angle of the DACT manufactured in the Saacke five-axis tool grinding center are 10.02° and 11.97°, respectively. The spiral angle at the cylindrical part is 30.11° and the flank face width is 0.793 mm.



(**a**) (**b**)

(**c**) (**d**)

Figure 13. Geometric parameters detection results of DACT: (**a**) rake angle of DACT; (**b**) relief angle of DACT; (**c**) spiral angle of DACT; (**d**) flank face width of DACT.



(**a**) (**b**)

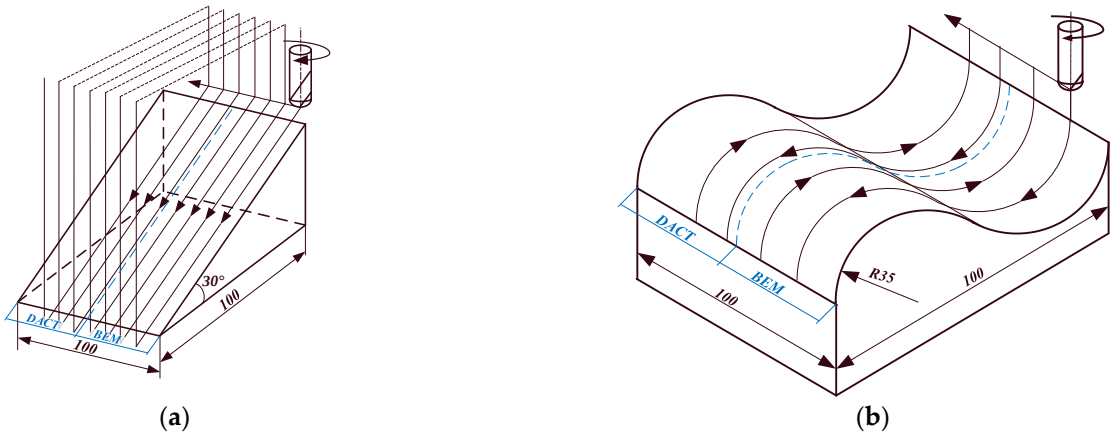
(**c**)

Figure 14. Tool accuracy testing equipment and accuracy testing results: (**a**) tool detection center; (**b**) Zoller operating system; (**c**) test results.

4. Study of the Cutting Performance of DACT

4.1. Experimental Conditions

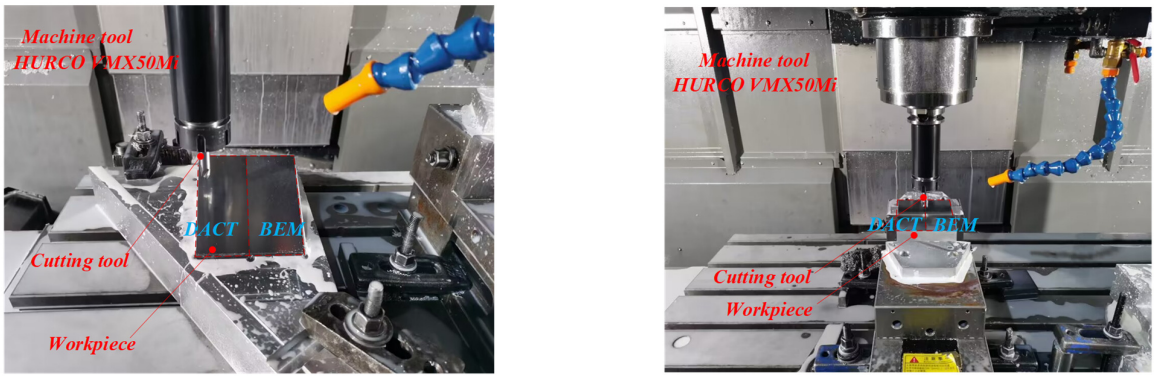
In this paper, contrast experiments were conducted to verify the applicability and advantages of the DACT compared with the BEM. The aluminum alloy labeled *7075T651* was selected as the workpiece material. The design surface of the workpiece includes two types: an inclined plane with the inclination angle $\alpha = 30°$, and a ruled surface with concave and convex surfaces. The specific construction sizes are shown in Figure 15.



(**a**) (**b**)

Figure 15. Milling mode of the workpieces: (**a**) inclined plane; (**b**) concave–convex ruled surface.

The milling experiments were conducted in a HURCO VMX50Mi three-axis NC milling machine, as shown in Figure 16. The axial cutting depth a_p was 0.2 mm, while the feed rate was 1500 mm/min. When milling the inclined plane, the path interval was 0.2 mm; when milling the ruled surface, the path interval was 0.1 mm.



(**a**) (**b**)

Figure 16. Machine tool and cutting tools: (**a**) inclined plane; (**b**) concave–convex ruled surface.

In addition, a Kister 9171A revolving dynamometer and a VDL-1000E machine were adopted in the test process to collect the cutting force, as shown in Figure 17.

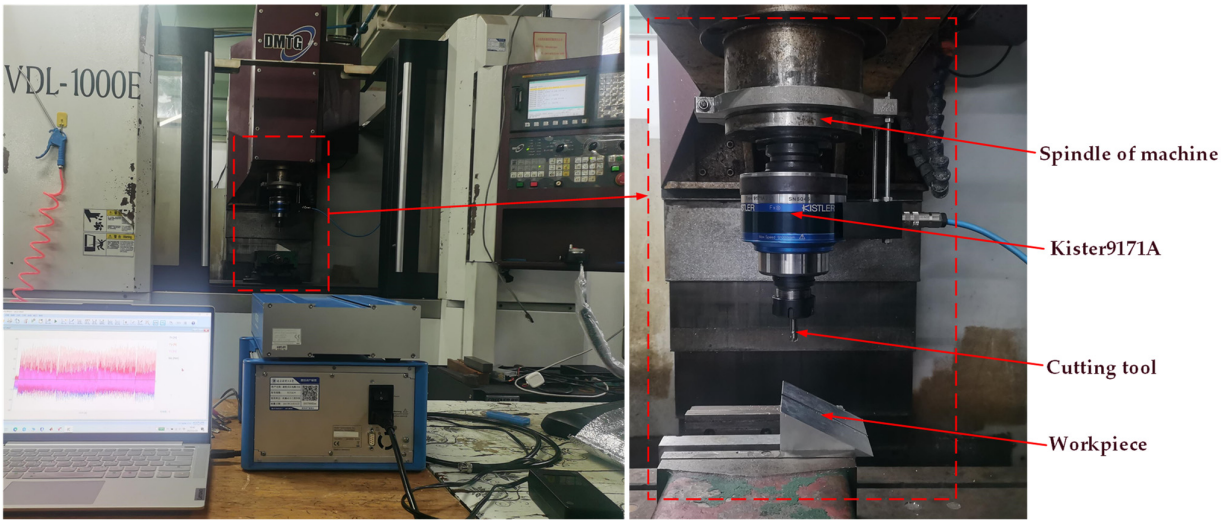


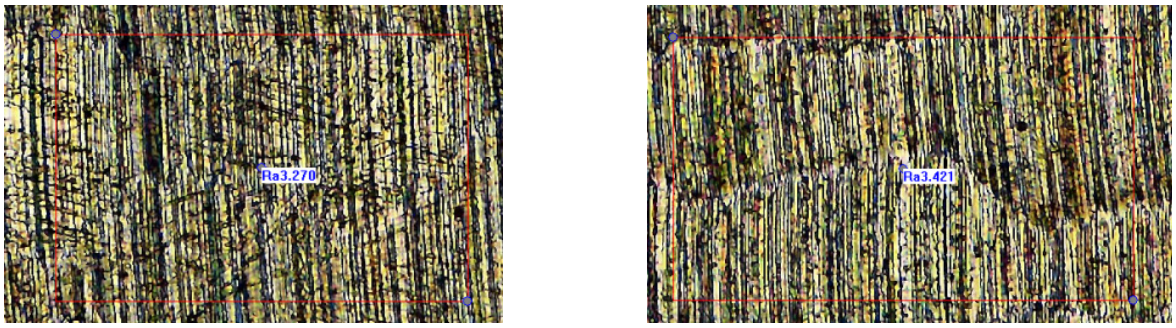
Figure 17. Cutting force test layout.

In the experiments, a PZ-CS3500A 3D microscope system with super depth of field was adopted to measure the experimental data.

4.2. Experimental Results and Conclusions

4.2.1. Milling of the Inclined Plane

The surface roughness of the inclined plane is shown in Figure 18. The surface roughness value machined by the DACT is *Ra*3.270, while the surface roughness value processed by the BEM is *Ra*3.421. When comparing the experimental results, the surface roughness value machined by the DACT is smaller, and the processing quality is better.



(**a**) (**b**)

Figure 18. Workpiece surface roughness: (**a**) workpiece machined by DACT; (**b**) workpiece machined by BEM.

The surface topography of the inclined plane machined by DACT and BEM are shown in Figures 19 and 20, respectively. The cross-section profile curve data of the inclined plane machined by the DACT and BEM were collected and drawn using MATLAB, as shown in Figure 21.

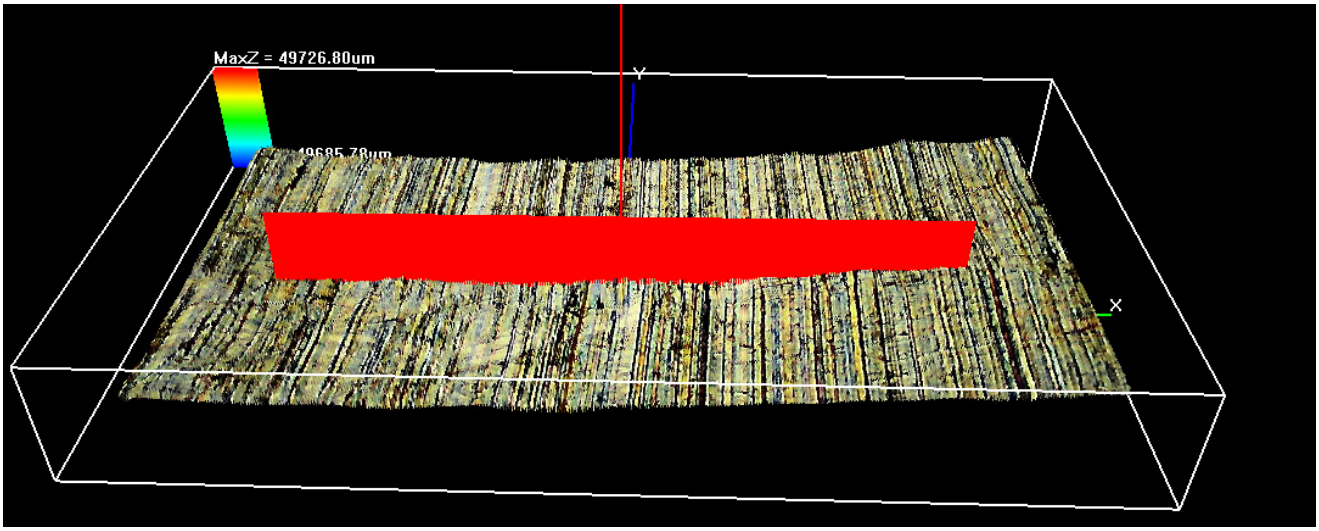


Figure 19. Workpiece surface topography machined by DACT.

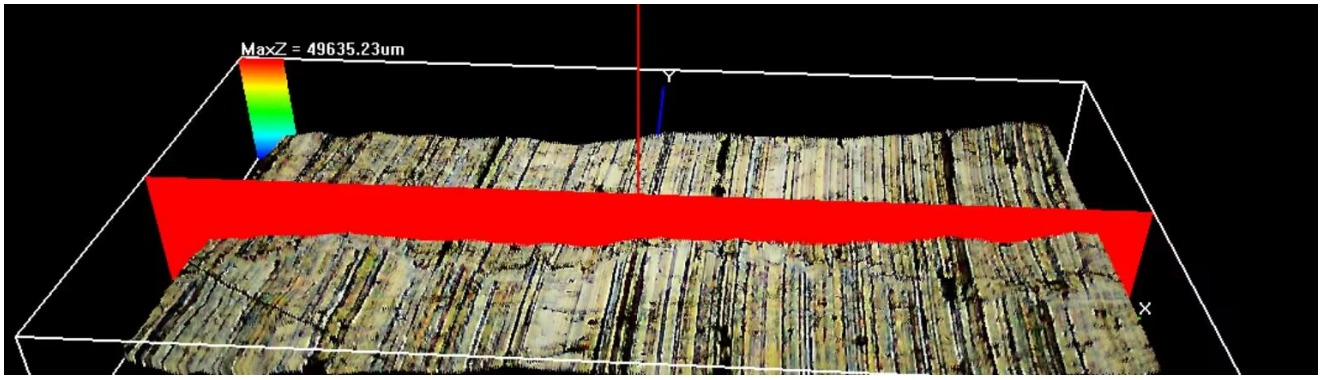


Figure 20. Workpiece surface topography machined by BEM.

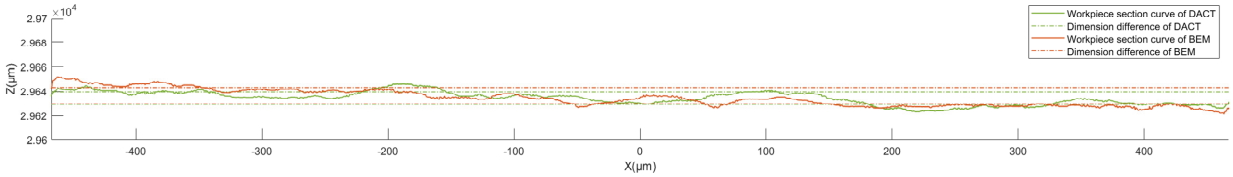


Figure 21. Comparison of workpiece cross section profile curve between DACT and BEM.

Through numerical analysis, the variance, the standard deviation, and the range of the cross-section profile curve data of the inclined plane machined by the DACT is 29.8403, 5.4626, and 22.3438, respectively. Meanwhile, the variance, the standard deviation, and the range of the cross-section profile curve data of the inclined plane machined by the BEM is 47.1185, 6.8643, and 30.2734, respectively.

It is obvious that the variance, the standard deviation, and the range of the cross-section profile curve data of the inclined plane machined by DACT are always smaller than by BEM; thus, better processing quality can be obtained when machining with the DACT.

The cutting force component F_x, F_y, and F_z in the direction of the X-axis, Y-axis, and Z-axis, respectively, of the DACT and BEM are shown in Figure 22, while the radial force F_{rad} and the resultant force F_{res} of the DACT and BEM are shown in Figure 23.

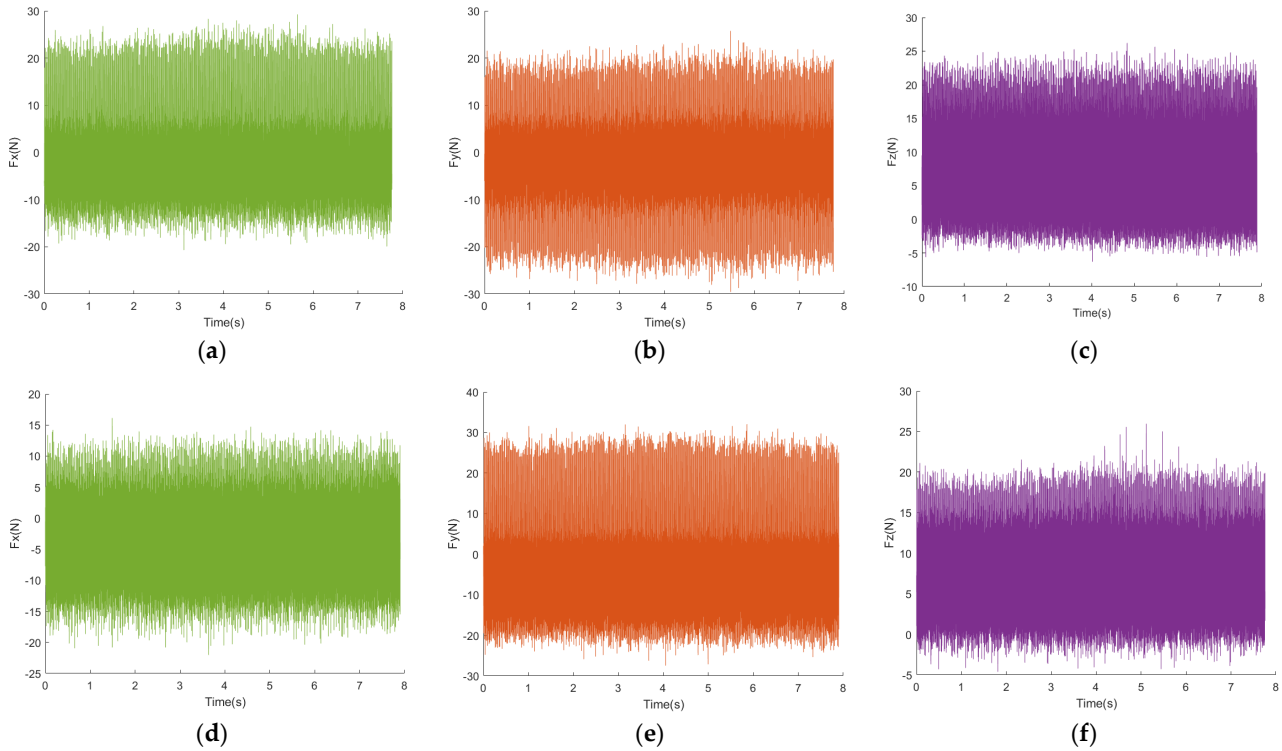


Figure 22. Cutting force: (**a**) F_x of DACT; (**b**) F_y of DACT; (**c**) F_z of DACT; (**d**) F_x of BEM; (**e**) F_y of BEM; (**f**) F_z of BEM.

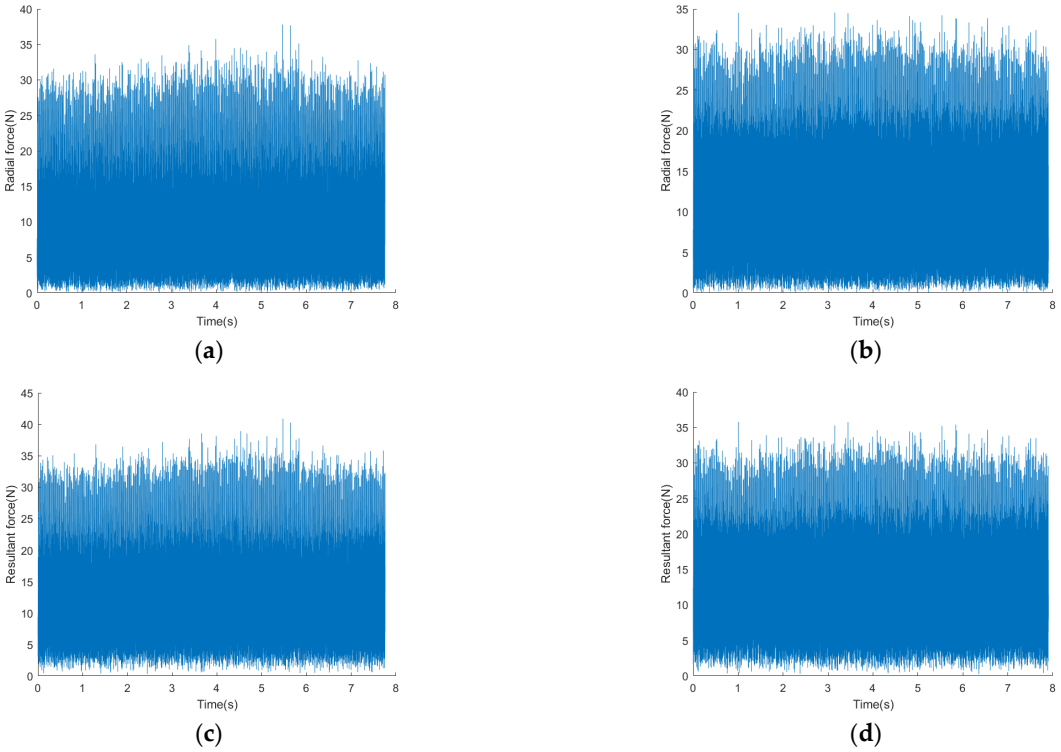


Figure 23. Cutting force: (**a**) radial force of DACT; (**b**) radial force of BEM; (**c**) resultant force of DACT; (**d**) resultant force of BEM.

The averages of F_x, F_y, F_z, F_{rad}, and F_{res} after data processing are listed in Table 2.

Table 2. Cutting force analysis.

Cutting Force	DACT	BEM
The averages of F_x (N)	6.5273	5.3025
The averages of F_y (N)	5.8546	7.3486
The averages of F_z (N)	6.3999	4.7959
The averages of F_{rad} (N)	9.3805	10.0048
F_z/F_{rad}	0.6823	0.4794
The averages of F_{res} (N)	12.0197	11.5580

The averages of F_x, F_y, F_z, F_{rad}, and F_{res} of the DACT and BEM are analyzed comprehensively. The experimental data show that the axial force F_z and the resultant force F_{res} of the DACT are larger than those of the BEM in this experiment. As mentioned in Section 2.2, the effective cutting width of the DACT is larger than that of the BEM by selecting an appropriate feed direction angle γ so that more materials can be removed. It is obvious that the feed direction angle γ is 0 in this experiment, and the cutting width of the DACT is the largest. Thus, more materials were removed and the resultant force F_{res} of the DACT is larger. Due to the tool cutting edge angle Kr of the DACT being smaller than the BEM, the axial force F_z of the DACT is larger than that of the BEM. At the same time, the radial force F_{rad} of the DACT is smaller than that of the BEM.

When analyzing the average of the axial force F_z and the radial force F_{rad} of the DACT and BEM, the ratios of F_z and F_{rad} are 0.6823 and 0.4794, respectively. The larger the ratio of F_z and F_{rad}, the better the process stability of the cutting tool. Therefore, the process stability of the DACT is better than the BEM in this experiment.

4.2.2. Milling of the Ruled Surface

The surface textures of the machined ruled surface are shown in Figure 24. The surface texture varies with the selected position of the ruled surface.

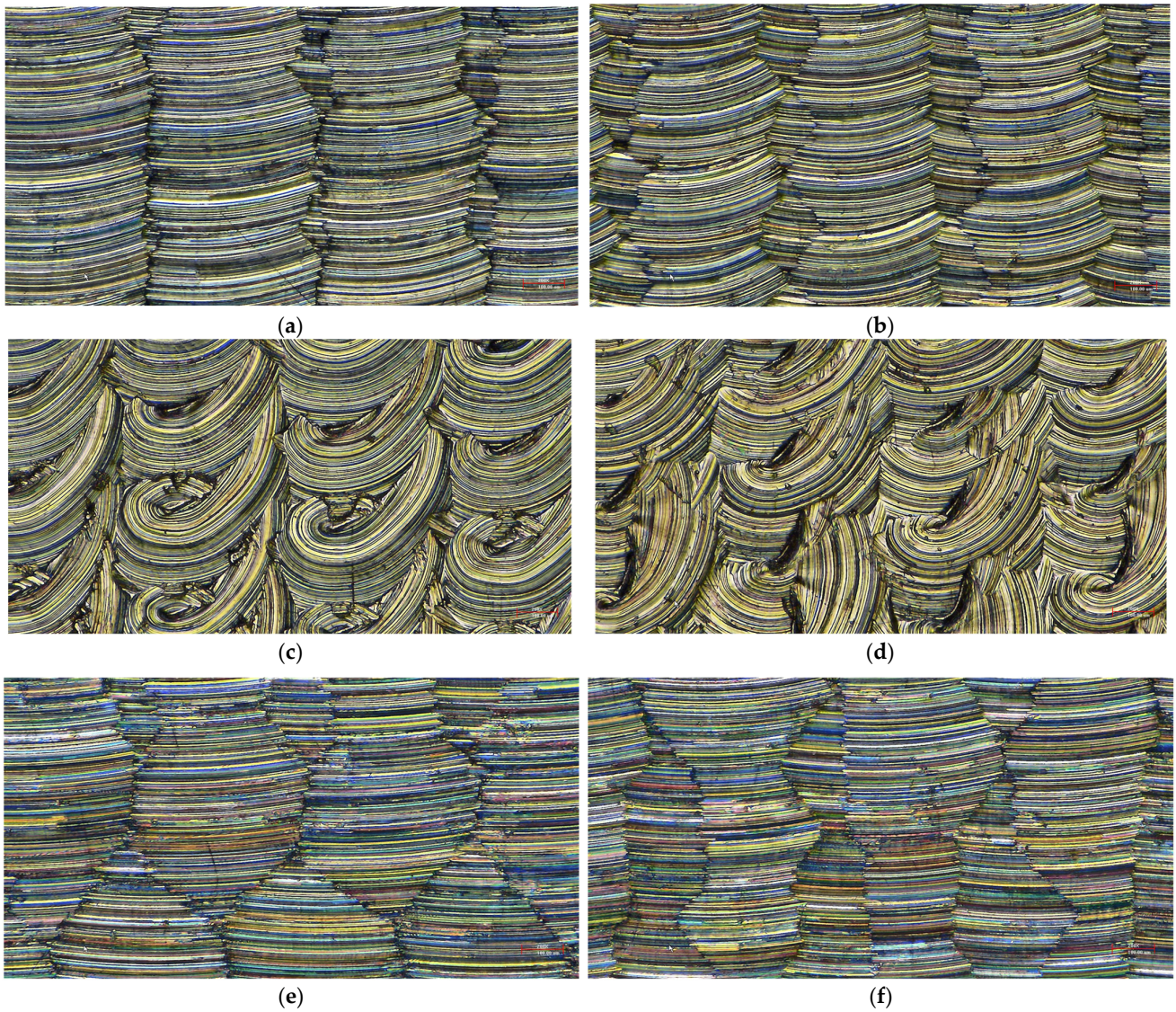


Figure 24. Comparison of workpiece surface between DACT and BEM: (**a**) surface machined by DACT with inclination angle of approximately 10°; (**b**) surface machined by BEM with inclination angle of approximately 10°; (**c**) surface machined by DACT with inclination angle of 0°; (**d**) surface machined by BEM with inclination angle of 0°; (**e**) surface machined by DACT with inclination angle of approximately 20°; (**f**) surface machined by BEM with inclination angle of approximately 20°.

The surface textures of the ruled surface machined by the DACT and BEM when selecting the position with an inclination angle of approximately 10° are shown in Figures 24a and 24b, respectively.

The surface textures of the ruled surface machined by the DACT and BEM when selecting the position with an inclination angle of 0° are shown in Figures 24c and 24d, respectively.

The surface textures of the ruled surface machined by the DACT and BEM when selecting the position with an inclination angle of approximately 20° are shown in Figures 24e and 24f, respectively.

Through comparison and analysis, it is obvious that the cutting splicing area between two tool paths of the DACT is smaller than that of the BEM. Consequently, the cutting scallop height of the DACT is always smaller than that of the BEM.

The surface topography of the ruled surface machined by the DACT and BEM are shown in Figures 25–28. The cross-section profile curves are shown in these figures as well. A set of the cross-section profile curve data taken from the ruled surface machined by the DACT and BEM were collected and drawn using MATLAB, as shown in Figure 29.

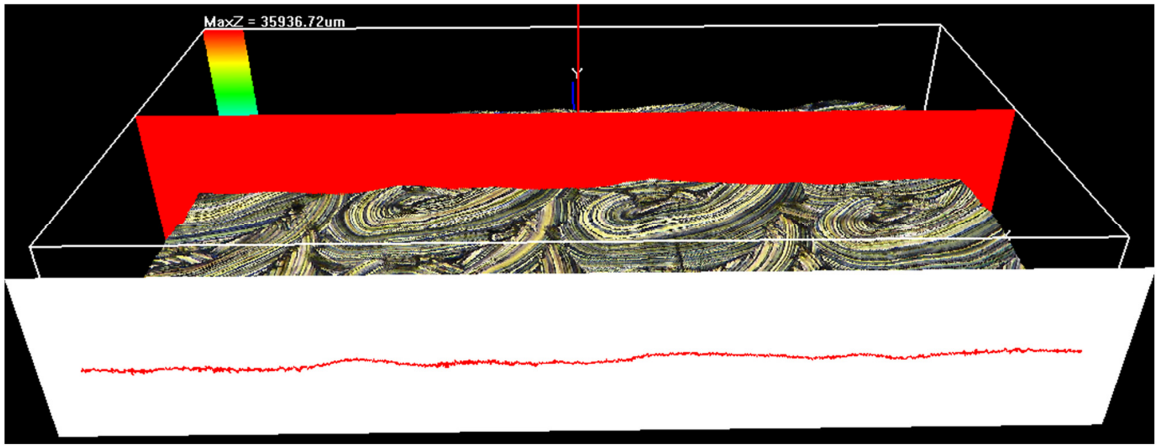


Figure 25. Workpiece surface topography machined by DACT with inclination angle of 0°.

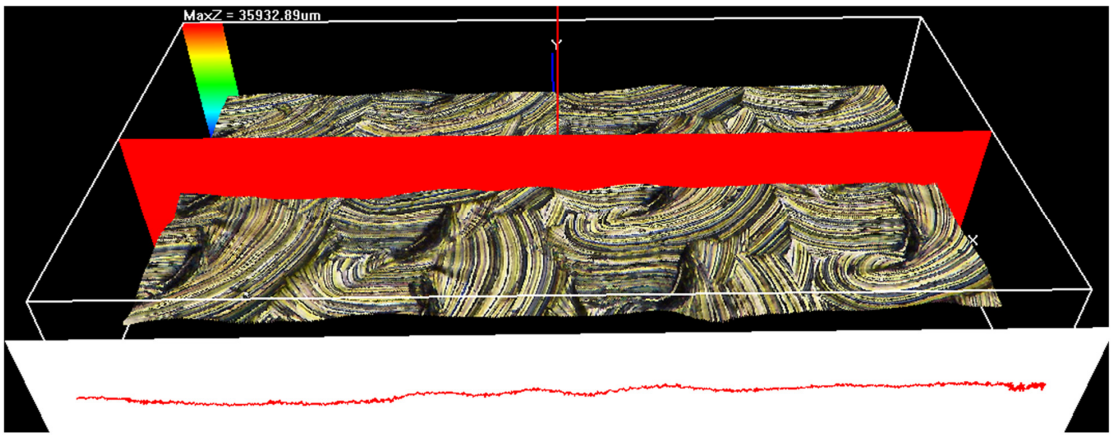


Figure 26. Workpiece surface topography machined by BEM with inclination angle of 0°.

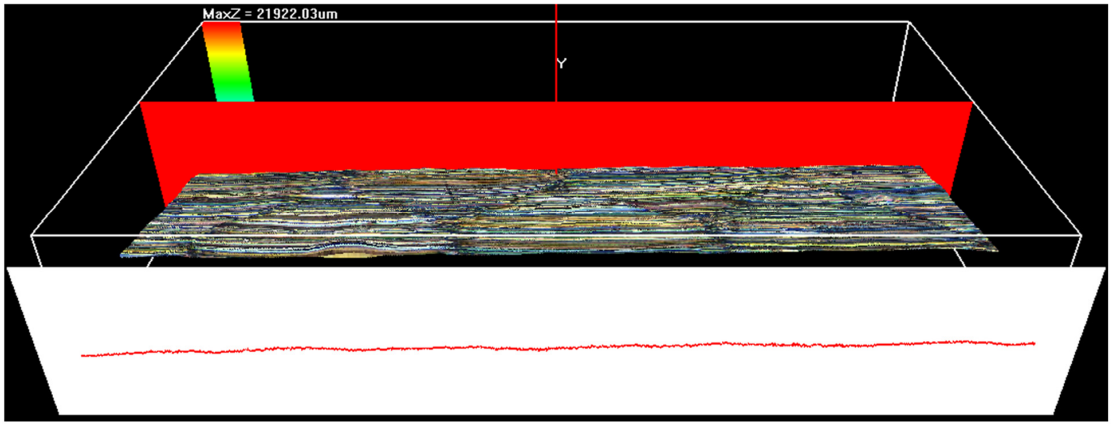


Figure 27. Workpiece surface topography machined by DACT with inclination angle of approximately 20°.

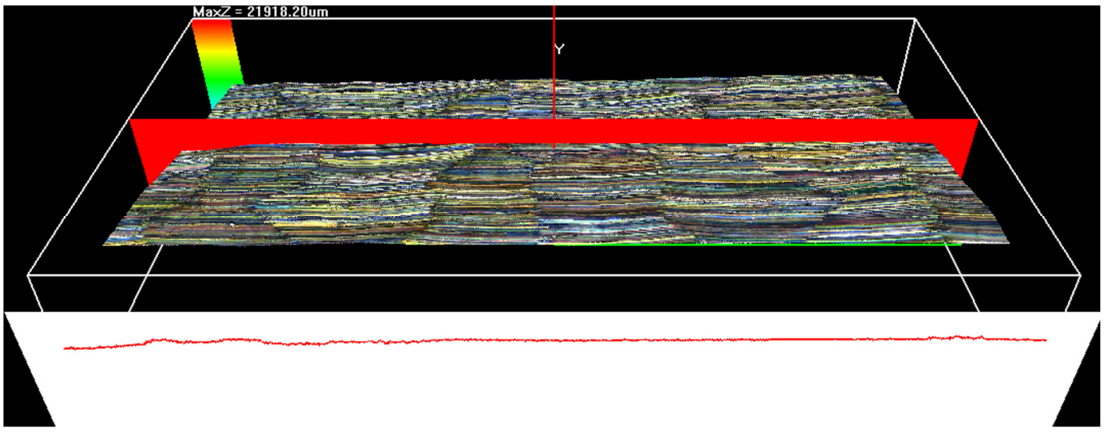


Figure 28. Workpiece surface topography machined by BEM with inclination angle of approximately 20°.

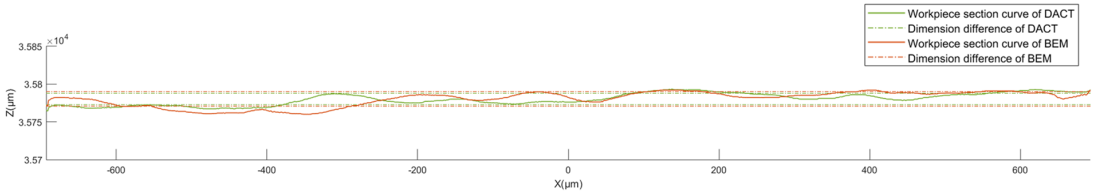


Figure 29. Standard deviation interval of concave and convex ruled surface.

Through numerical analysis, the variance, the standard deviation, and the range of the cross-section profile curve data taken from the ruled surface machined by the DACT is 58.0884, 7.6216, and 29.1406, respectively. Meanwhile, the variance, the standard deviation, and the range of the cross-section profile curve data taken from the ruled surface machined by the BEM is 92.7146, 9.6288, and 31.9336, respectively.

It is obvious that the variance, the standard deviation, and the range of the cross-section profile curve data taken from the ruled surface machined by the DACT are always smaller than for the BEM; thus, better processing quality can be obtained when machining with the DACT.

5. Conclusions

1. Through the innovative design of the profile surface, a double-arc cutting tool is developed. Three types of cutting edge curves are proposed (cutting edge with a constant helix angle, cutting edge with a constant pitch, and the orthogonal spiral cutting edge). The effective cutting speed of the DACT is always higher than that of the BEM.
2. The effective cutting width of the DACT is larger than that of the BEM when selecting an appropriate feed direction angle γ. Meanwhile, the cutting scallop height of the DACT is always smaller than that of the BEM, so that more materials can be removed. The DACT is more suitable for machining surfaces with a small curvature.
3. Through the comparative analysis of the surface roughness and surface textures of the machined workpiece, the surface roughness value of the DACT is smaller and the cutting splicing area between the two tool paths of the DACT is also smaller than that of the BEM. Thus, better processing quality can be obtained when machining with the DACT.

Author Contributions: Conceptualization, M.F. and X.L.; methodology, M.F. and C.B.; software, M.F. and C.B.; validation, M.F. and C.Y.; investigation, Y.Z.; resources, X.L. and Y.Z.; data curation, M.F. and C.Y.; writing—original draft preparation, C.B.; writing—review and editing, M.F. and C.Y.; supervision, C.Y.; project administration, X.L.; funding acquisition, X.L. All authors have read and agreed to the published version of the manuscript.

Funding: This research was funded by National Nature Science Foundation of China, U22A20128; and Natural Science Foundation of Heilongjiang Province of China, TD2022E003.

Institutional Review Board Statement: Not applicable.

Informed Consent Statement: Not applicable.

Conflicts of Interest: The authors declare no conflict of interest.

References

1. Ghorbani, M.; Movahhedy, M.R. An analytical model for cutter-workpiece engagement calculation in ball-end finish milling of doubly curved surfaces. *Int. J. Adv. Manuf. Technol.* **2019**, *102*, 1635–1657. [CrossRef]
2. Li, S.; Dong, Y.; Li, Y.; Li, P.; Yang, Z.; Landers, R.G. Geometrical simulation and analysis of ball-end milling surface topography. *Int. J. Adv. Manuf. Technol.* **2019**, *102*, 5–8.
3. Chen, T.; Li, R.; Xiang, J.P.; Gao, W.J.; Wang, Y.S. Study on the design and cutting performance of stepped bi-directional milling cutters for hole making of CFRP. *Int. J. Adv. Manuf. Technol.* **2020**, *108*, 3.
4. Patel, K.; Bolaños, G.; Bolaños, R.; Bedi, S. Optimal tool shape selection based on surface geometry for three-axis CNC machining. *Int. J. Adv. Manuf. Technol.* **2011**, *57*, 5–8. [CrossRef]
5. Otkur, M.; Lazoglu, I. Trochoidal milling. *Int. J. Mach. Tools. Manuf.* **2007**, *47*, 1324–1332. [CrossRef]
6. Yang, Y.Q.; Wang, Y.F.; Liu, Q. Design of a milling cutter with large length–diameter ratio based on embedded passive damper. *J. Vib. Control.* **2019**, *25*, 3. [CrossRef]
7. Basso, I.; Voigt, R.; Rodrigues, A.R.; Marin, F.; De, S.A.F.; De Lacalle, L.N.L. Influences of the workpiece material and the tool-surface engagement (TSE) on surface finishing when ball-end milling. *J. Manuf. Process.* **2022**, *75*, 219–231. [CrossRef]
8. Yang, S.C.; He, C.S.; Zheng, M.L. A prediction model for titanium alloy surface roughness when milling with micro-textured ball-end cutters at different workpiece inclination angles. *Int. J. Adv. Manuf. Technol.* **2019**, *100*, 2115–2122.
9. Cheng, X.F.; Ding, G.F.; Li, R.; Ma, X.J.; Qin, S.F.; Song, X.L. A new design and grinding algorithm for ball-end milling cutter with tooth offset center. *Proc. Inst. Mech. Eng. Part B J. Eng. Manuf.* **2014**, *228*, 687–697. [CrossRef]
10. Masahiko, J.; Isamu, G.; Takeshi, W.; Jun-ichi, K.; Masao, M. Development of CBN ball-nosed end mill with newly designed cutting edge. *J. Mater. Process. Technol.* **2007**, *192–193*, 48–54.
11. Li, T.; Chen, W.Y.; Xu, R.F.; Wang, D. Flank milling for blisk with a barrel ball milling cutter. *Key Eng. Mater.* **2009**, *407–408*, 202–206. [CrossRef]
12. Wang, G.Y.; Liu, X.L.; Chen, T.; Gao, W.J. An Experimental Study on Milling Titanium Alloy with a Revolving Cycloid Milling Cutter. *Appl. Sci.* **2020**, *10*, 4. [CrossRef]
13. Liu, X.L.; Tong, X.; Yang, S.C.; He, C.S.; Liu, X. Models of the relationship among geometric parameters and anti-friction mechanism of micro-texture ball-end milling cutter. *Adv. Mech.* **2018**, *10*, 6. [CrossRef]
14. Zhang, W.; Zhang, L.; Wang, B.; Wang, S.Q. Finite element simulation analysis of bionic ball-end milling cutter. *Int. J. Adv. Manuf. Technol.* **2019**, *103*, 5–8. [CrossRef]
15. Chang, H.B.; Li, S.Y.; Shi, R.P. Design and Manufacturing Technology of High Speed Milling Cutter for Aluminum Alloy. *Procedia Eng.* **2017**, *174*, 630–637. [CrossRef]
16. Liu, X.L.; Jiang, Z.P.; Li, M.Y.; Ding, Y.P.; Wang, G.Y.; Liu, L.J. New round end milling cutter for mold processing based on residual height design. *J. Chin. J. Mech. Eng.* **2015**, *51*, 192–204. [CrossRef]
17. Guo, M.L.; Wei, Z.C.; Gao, H.; Zhang, Z.H.; Jiang, J. New Left-Handed Milling Cutter and Process for Burrs-Free Machining of Precision Copper Electrode. *J. Manuf. Sci. Eng.* **2023**, *145*, 2. [CrossRef]
18. Zhao, Z.Y.; Wang, S.B.; Wang, S.L.; Wang, Z.H.; Huang, Q.; Yang, B. Ball-end milling cutter design method towards the maximum material removal rate under surface roughness constraints. *J. Manuf. Process.* **2022**, *78*, 254–264. [CrossRef]
19. Bi, G.J.; Wang, F.J.; Fu, R.; Chen, P.Z. Wear characteristics of multi-tooth milling cutter in milling CFRP and its impact on machining performance. *J. Manuf. Process.* **2022**, *81*, 580–593. [CrossRef]
20. Itoh, M.; Hayasaka, T.; Shamoto, E. High-efficiency smooth-surface high-chatter-stability machining of thin plates with novel face-milling cutter geometry. *Precis. Eng.* **2020**, *64*, 165–176. [CrossRef]
21. Li, M.Y.; Zhao, W.; Liang, L.; He, N.; Muhammad, J. Chatter Suppression during Milling of Ti-6Al-4V Based on Variable Pitch Tool and Process Damping Effect. *Machines* **2022**, *10*, 222. [CrossRef]
22. Lee, S.H.; Lan, T.S.; Chen, Y.T.; Chen, W. Design and NC Machining of Ball-End Taper Cutter with Constant Pitch. *J. Appl. Sci.* **2008**, *8*, 4. [CrossRef]
23. Berend, D.; Benjamin, B.; Mirko, T.; Philipp, W. Geometrical process design during continuous generating grinding of cutting tools. *Int. J. Adv. Manuf. Technol.* **2022**, *121*, 5–6.
24. Yang, S.C.; Su, S.A.; Liu, X.L.; Han, P. Study on Milling Temperature of Titanium Alloy with Micro-Textured Ball End Milling Cutter under Radius of Blunt Edge. *Appl. Sci.* **2020**, *10*, 587. [CrossRef]

25. Wang, G.Y.; Liu, X.L.; Gao, W.J.; Yan, B.X.; Chen, T. Study on the Design and Cutting Performance of a Revolving Cycloid Milling Cutter. *Appl. Sci.* **2019**, *9*, 2915. [CrossRef]
26. Puma-Araujo, S.D.; Olvera-Trejo, D.; Martínez-Romero, O.; Urbikain, G.; Elías-Zúñiga, A.; De Lacalle, L.N.L. Semi-Active Magnetorheological Damper Device for Chatter Mitigation during Milling of Thin-Floor Components. *Appl. Sci.* **2020**, *10*, 5313. [CrossRef]

Disclaimer/Publisher's Note: The statements, opinions and data contained in all publications are solely those of the individual author(s) and contributor(s) and not of MDPI and/or the editor(s). MDPI and/or the editor(s) disclaim responsibility for any injury to people or property resulting from any ideas, methods, instructions or products referred to in the content.